

# Diffraction Tomography, Fourier Reconstruction, and Full Waveform Inversion

Florian Faucher<sup>1</sup>      Clemens Kirisits<sup>1</sup>      Michael Quellmalz<sup>2</sup>  
[florian.faucher@univie.ac.at](mailto:florian.faucher@univie.ac.at)      [clemens.kirisits@univie.ac.at](mailto:clemens.kirisits@univie.ac.at)      [quellmalz@math.tu-berlin.de](mailto:quellmalz@math.tu-berlin.de)  
 Otmar Scherzer<sup>1,3</sup>      Eric Setterqvist<sup>3</sup>  
[otmar.scherzer@univie.ac.at](mailto:otmar.scherzer@univie.ac.at)      [eric.setterqvist@ricam.oeaw.ac.at](mailto:eric.setterqvist@ricam.oeaw.ac.at)

October 18, 2021

<sup>1</sup>Faculty of Mathematics  
 University of Vienna  
 Oskar-Morgenstern-Platz 1  
 A-1090 Vienna, Austria

<sup>2</sup>Institute of Mathematics  
 Technical University Berlin  
 Straße des 17. Juni 136  
 D-10623 Berlin, Germany

<sup>3</sup>Johann Radon Institute for Computational and Applied Mathematics (RICAM)  
 Altenbergerstraße 69  
 A-4040 Linz, Austria

## Abstract

In this paper, we study the mathematical imaging problem of diffraction tomography (DT), which is an inverse scattering technique used to find material properties of an object by illuminating it with probing waves and recording the scattered waves. Conventional DT relies on the Fourier diffraction theorem, which is applicable under the condition of weak scattering. However, if the object has high contrasts or is too large compared to the wavelength, it tends to produce multiple scattering, which complicates the reconstruction. We give a survey on diffraction tomography and compare the reconstruction of low and high contrast objects. We also implement and compare the reconstruction using the full waveform inversion method which, contrary to the Born and Rytov approximations, works with the total field and is more robust to multiple scattering.

## 1. INTRODUCTION

*Diffraction tomography* (DT) is a technique for reconstructing the scattering potential of an object from measurements of waves scattered by that object. DT can be understood as an alternative to, or extension of, classical computerized tomography. In computerized tomography a crucial assumption is that the radiation, typically X-rays, essentially propagates along straight lines through the object. The attenuated rays are recorded and can be related to material properties  $f$  of the object by means of the Radon transform. A central result for the inversion of this relation is the Fourier slice theorem. Roughly speaking, it says that the Fourier transformed measurements are equal to the Fourier transform of  $f$  evaluated along slices through the origin.

The straight ray assumption of computerized tomography can be considered valid as long as the wavelength of the incident field is much smaller than the size of the relevant details in the object.

As soon as the wavelength is similar to or greater than those details, for instance in situations where X-rays are replaced by visible light, diffraction effects are no longer negligible. As an example of a medical application, an optical diffraction experiment in [47] utilized a red laser of wavelength 633 nm to illuminate human cells of diameter around 10  $\mu\text{m}$ , which include smaller subcellular organelles. One way to achieve better reconstruction quality in such cases is to drop the straight ray assumption and adopt a propagation model based on the wave equation instead.

The theoretical groundwork for DT was laid more than half a century ago by Wolf [51]. The central result derived there, sometimes called the *Fourier diffraction theorem*, says that the Fourier transformed measurements of the scattered wave are equal to the Fourier transform of the scattering potential evaluated along a hemisphere. This result relies on a series of assumptions: (i) the object is immersed in a homogeneous background, (ii) the incident field is a monochromatic plane wave, (iii) the scattered wave is measured on a plane in  $\mathbb{R}^3$ , and (iv) the first Born approximation of the scattered field is valid.

On the one hand the Born approximation greatly simplifies the relationship between scattered wave and scattering potential. On the other hand, however, it generally requires the object to be weakly scattering, thus limiting the applicability of the Fourier diffraction theorem. An alternative is to assume validity of the first Rytov approximation instead [25]. While mathematically this amounts to essentially the same reconstruction problem, the underlying physical assumptions are not identical to those of the Born approximation, leading to a different range of applicability in general [6, 46]. Nevertheless, the restriction to weakly scattering objects remains.

*Full waveform inversion* (FWI) is a different approach that can overcome some of the limitations of the first-order methods, typically at the cost of being computationally more demanding. It relies on the iterative minimization of a cost functional which penalizes the misfit between measurements and forward simulations of the total field, cf. [2, 33, 43, 48, 50]. Here, the forward model consists of the solution of the full wave equation, without simplification of first-order approximations. In our implementation of FWI, we do not rely on model simplifications for establishing an explicit expression of the unknown in terms of the data but instead consider the full model, i.e., we perform nonlinear minimization.

**Contribution and outline.** In this chapter we present a numerical comparison of three reconstruction approaches for diffraction tomography on simulated data, based on (i) the Born approximation, (ii) the Rytov approximation, and (iii) FWI. The setting we use for this comparison is 2D transmission imaging in a homogeneous background with (approximate) plane wave irradiation. The object is assumed to make a full turn during the experiment, providing measurements for a uniform set of incidence angles. In addition we investigate how providing additional data by varying the wavelength affects the reconstruction. The scattering potentials considered here are test phantoms of varying sizes, shapes, and contrasts. Moreover, for data generation purposes we compare several forward models.

For numerical reconstruction under the Born and Rytov approximations a well-known method is the backpropagation algorithm [10], which is widely used in practice, cf. [37] and also [12]. Our algorithms rely on the nonuniform discrete Fourier transform (NDFT), which was used in 3D Fourier diffraction tomography yielding better results than discrete backpropagation [30]. Nonuniform Fourier methods have also been applied in computerized tomography [42], magnetic resonance imaging [31], spherical tomography [23, 24] or surface wave tomography [22]. Our FWI-based reconstruction uses an iterative Newton-type method on an  $L^2$  distance between data and simulations. For the discretization of the resulting partial differential equations, we use

the hybridizable discontinuous Galerkin method (HDG), [8, 18], and the open-source parallel software `hawen`<sup>1</sup>, [14].

The outline of this chapter is as follows. The conceptual experiment is detailed in Section 2. Forward models are presented in Section 3, and their numerical performance is compared in Section 4. The Fourier diffraction theorem is formulated and discussed in Section 5. Further, Section 6 covers the reconstruction algorithms used for the numerical experiments, which are presented in Section 7. A concluding discussion of our findings is given in Section 8.

## 2. EXPERIMENTAL SETUP

We consider the tomographic reconstruction of a two-dimensional object taking into account diffraction of the incident field. The object is assumed to be embedded in a homogeneous background and illuminated or insonified by a monochromatic plane wave. In fact, for the computational experiments, we implement and compare several approaches to approximate the incident plane wave, see Section 4. We restrict ourselves to transmission imaging, where the incident field propagates in direction  $\mathbf{s}$  and the resulting field is measured on the line  $\mathbf{x} \cdot \mathbf{s} = r_M$ . The distance between the *measurement line* and the origin,  $r_M > 0$ , is sufficiently large so that it does not intersect the object. From the measurements, we aim to reconstruct the object's scattering properties. In order to improve the reconstruction quality, we generate additional data by rotating the object or changing the incident field's wavelength. See Figure 1 for an illustration of the experimental setup.

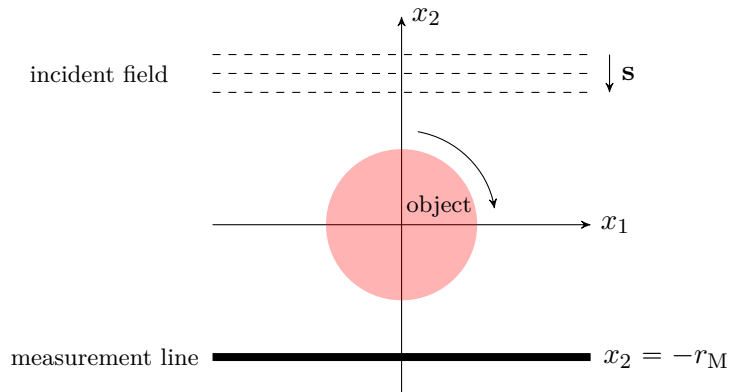


FIGURE 1. Experimental setup with incidence direction  $\mathbf{s} = (0, -1)^\top$  and measurement line located at  $x_2 = -r_M$ .

We now introduce the physical quantities needed subsequently. Let  $\lambda > 0$  denote the *wavelength* of the incident wave and  $k_0 = 2\pi/\lambda$  the *wave number*. Furthermore, let  $n(\mathbf{x})$  denote the *refractive index* at position  $\mathbf{x} \in \mathbb{R}^2$  and  $n_0$  the constant refractive index of the background. From these quantities, we define

$$k(\mathbf{x}) := k_0 \frac{n(\mathbf{x})}{n_0}. \quad (2.1)$$

The *scattering potential*  $f$  is given by

$$f(\mathbf{x}) := k^2(\mathbf{x}) - k_0^2 = k_0^2 \left( \frac{n(\mathbf{x})^2}{n_0^2} - 1 \right), \quad (2.2)$$

<sup>1</sup><https://ffaucher.gitlab.io/hawen-website/>

and is the quantity to be reconstructed from the measured data. Note that, for all practical purposes,  $f$  can be assumed to be bounded and compactly supported in the disk  $\mathcal{B}_{r_M} = \{\mathbf{x} \in \mathbb{R}^2 : \|\mathbf{x}\| < r_M\}$ .

### 3. FORWARD MODELS

In this section, we investigate several forward models for the experiment presented above. For all of them, the starting point is the system of equations

$$\begin{cases} (-\Delta - k^2) u^{\text{tot}} = g, \\ (-\Delta - k_0^2) u^{\text{inc}} = g, \\ u^{\text{tot}} = u^{\text{inc}} + u^{\text{sca}}. \end{cases} \quad (3.1)$$

Here,  $u^{\text{inc}}$  is the given *incident field*, the *total field*  $u^{\text{tot}}$  is what is recorded on the measurement line, and the difference between the two constitutes the *scattered field*  $u^{\text{sca}}$ . The models considered below are based on the following specifications of [Equation 3.1](#):

- (i) no source ( $g = 0$ ) and  $u^{\text{inc}}$  is an ideal plane wave, see [Equation 3.2](#),
- (ii) no source,  $u^{\text{inc}}$  is an ideal plane wave and  $u^{\text{sca}}$  satisfies the Born approximation,
- (iii) no source,  $u^{\text{inc}}$  is an ideal plane wave and  $u^{\text{sca}}$  satisfies the Rytov approximation,
- (iv)  $g$  represents a point source located far from the object,
- (v)  $g$  represents simultaneous point sources positioned along a straight line: we refer to this configuration as a ‘line source’.

**3.1. Incident plane wave.** First, we consider data in the ideal context of an incident monochromatic plane wave

$$u^{\text{inc}}(\mathbf{x}) = e^{ik_0\mathbf{x}\cdot\mathbf{s}}. \quad (3.2)$$

In this case, we obtain the following equation for the scattered field:

$$(-\Delta - k(\mathbf{x})^2) u^{\text{sca}}(\mathbf{x}) = f(\mathbf{x}) e^{ik_0\mathbf{x}\cdot\mathbf{s}}. \quad (3.3)$$

**3.1.1. The Born approximation.** [Equation 3.3](#) can be written as

$$(-\Delta - k_0^2) u^{\text{sca}}(\mathbf{x}) = f(\mathbf{x}) \left( e^{ik_0\mathbf{x}\cdot\mathbf{s}} + u^{\text{sca}}(\mathbf{x}) \right).$$

If the scattered field is negligible compared to the incident field, we can drop  $u^{\text{sca}}$  on the right-hand side and obtain,

$$(-\Delta - k_0^2) u^{\text{Born}}(\mathbf{x}) = f(\mathbf{x}) e^{ik_0\mathbf{x}\cdot\mathbf{s}}, \quad (3.4)$$

where  $u^{\text{Born}}$  is the *Born approximation* to the scattered field. Supplementing this equation with the Sommerfeld radiation condition we have a unique solution corresponding to an outgoing wave. It can be written as a convolution

$$u^{\text{Born}}(\mathbf{x}) = \int_{\mathbb{R}^2} G(\mathbf{x} - \mathbf{y}) f(\mathbf{y}) e^{ik_0\mathbf{y}\cdot\mathbf{s}} d\mathbf{y}, \quad (3.5)$$

where  $G$  is the outgoing Green's function for the Helmholtz equation. In  $\mathbb{R}^2$ , it is given by

$$G(\mathbf{x}) = \frac{i}{4} H_0^{(1)}(k_0 \|\mathbf{x}\|), \quad \mathbf{x} \in \mathbb{R}^2 \setminus \{\mathbf{0}\}, \quad (3.6)$$

where  $H_0^{(1)}$  denotes the zeroth order Hankel function of the first kind, see [9, Sect. 3.4]. We note that, in spite of a singularity at the origin,  $G$  is locally integrable in  $\mathbb{R}^2$ .

**3.1.2. The Rytov approximation.** In this subsection, we derive an alternative approximation for the scattered field. Introducing the complex phases  $\varphi^{\text{inc}}$ ,  $\varphi^{\text{tot}}$  and  $\varphi^{\text{sca}}$  according to

$$u^{\text{tot}} = e^{\varphi^{\text{tot}}}, \quad u^{\text{inc}} = e^{\varphi^{\text{inc}}}, \quad \varphi^{\text{tot}} = \varphi^{\text{inc}} + \varphi^{\text{sca}}, \quad (3.7)$$

one can derive from Equation 3.1, with  $g = 0$ , the following relation

$$(-\Delta - k_0^2)(u^{\text{inc}} \varphi^{\text{sca}}) = \left( f + (\nabla \varphi^{\text{sca}})^2 \right) u^{\text{inc}}, \quad (3.8)$$

where  $(\nabla \varphi^{\text{sca}})^2 = (\partial \varphi^{\text{sca}} / \partial x_1)^2 + (\partial \varphi^{\text{sca}} / \partial x_2)^2$ . The details of this derivation can be found, for instance, in [26, Sect. 6.2.2]. Neglecting  $(\nabla \varphi^{\text{sca}})^2$  in Equation 3.8 we obtain

$$(-\Delta - k_0^2)(u^{\text{inc}} \varphi^{\text{Rytov}}) = f u^{\text{inc}}, \quad (3.9)$$

where  $\varphi^{\text{Rytov}}$  is the *Rytov approximation* to  $\varphi^{\text{sca}}$ . Note that we still assume  $u^{\text{inc}}$  to be a monochromatic plane wave, as given in Equation 3.2. Thus the product  $u^{\text{inc}} \varphi^{\text{Rytov}}$  solves the same equation as  $u^{\text{Born}}$ . If we define the Rytov approximation to the scattered field,  $u^{\text{Rytov}}$ , in analogy to Equation 3.7 via

$$u^{\text{Rytov}} = e^{\varphi^{\text{Rytov}} + \varphi^{\text{inc}}} - u^{\text{inc}},$$

and replace  $\varphi^{\text{Rytov}}$  by  $\frac{u^{\text{Born}}}{u^{\text{inc}}}$ , we obtain a relation between the two approximate scattered fields that can be expressed as

$$u^{\text{Born}} = u^{\text{inc}} \log \left( \frac{u^{\text{Rytov}}}{u^{\text{inc}}} + 1 \right). \quad (3.10)$$

**Remark 3.1** There have been many investigations about the validity of the Born and Rytov approximations, see, e.g., [6, 46] or [26, chap. 6]. The Born approximation is reasonable only for relatively a small object. In particular, for a homogeneous cylinder of radius  $a$ , the Born approximation is valid if  $a(n - n_0) < \lambda/4$ , where  $\lambda$  is the wavelength of the incident wave and  $n$  is the constant refractive index inside the object. In contrast, the Rytov approximation only requires that  $n - n_0 > (\nabla \varphi^{\text{sca}})^2 / k_0^2$ , i.e., the phase change of the scattered phase  $\varphi^{\text{sca}}$ , see Equation 3.7, is small over one wavelength, but it has no direct requirements on the object size and is therefore applicable for a larger class of objects. The latter is also observed in numerical simulations in [6]. However, for objects that are small and have a low contrast  $n - n_0$ , the Born and Rytov approximation produce approximately the same results.

**3.2. Modeling the total field using line and point sources.** As an alternative to ideal incident plane waves we consider models with one or several point sources. If arranged the right way, the resulting incident field can resemble a monochromatic plane wave. We expect that such models might be more representative of actual experiments, where the source is localized (e.g., transducers).

**3.2.1. Point source far from object.** In this case the right-hand side in [Equation 3.1](#) is a Dirac delta function so that we obtain

$$\begin{cases} (-\Delta - k(\mathbf{x})^2) u_{\text{P}}^{\text{tot}}(\mathbf{x}) = \delta(\mathbf{x} - \mathbf{x}_0), \\ (-\Delta - k_0^2) u_{\text{P}}^{\text{inc}}(\mathbf{x}) = \delta(\mathbf{x} - \mathbf{x}_0). \end{cases} \quad (3.11)$$

If the position of the source,  $\mathbf{x}_0$ , is sufficiently far from the origin, then, after appropriate rescaling,  $u_{\text{P}}^{\text{inc}}$  approximates a plane wave with wave number  $k_0$  and propagation direction  $\mathbf{s} = -\mathbf{x}_0 / \|\mathbf{x}_0\|$  in a neighborhood of  $\mathbf{0}$ . We refer to [Section 4](#) for a numerical comparison of the different models presented here.

**3.2.2. Line source.** Alternatively, we let  $g$  be a sum of Dirac functions and consider

$$\begin{cases} (-\Delta - k(\mathbf{x})^2) u_{\text{L}}^{\text{tot}}(\mathbf{x}) = \sum_{j=1}^{N_{\text{sim}}} \delta(\mathbf{x} - \mathbf{x}_j), \\ (-\Delta - k_0^2) u_{\text{L}}^{\text{inc}}(\mathbf{x}) = \sum_{j=1}^{N_{\text{sim}}} \delta(\mathbf{x} - \mathbf{x}_j), \end{cases} \quad (3.12)$$

where the number  $N_{\text{sim}}$  of simultaneous point sources should be sufficiently large. Moreover, the positions  $\mathbf{x}_j$  should be arranged uniformly along a line perpendicular to the propagation direction  $\mathbf{s}$  of the plane wave. See [Section 4.2](#).

## 4. NUMERICAL COMPARISON OF FORWARD MODELS

In this section, we numerically compare the forward models presented above. For the discretization of the partial differential equation, we use the *hybridizable discontinuous Galerkin method* (HDG), [\[8, 18\]](#), and the open-source parallel software `hawen`, see [\[14\]](#) and [footnote 1](#). It is further employed to carry out the reconstruction with FWI in [Section 6.1](#).

Both for plane waves and point sources, we consider wave propagation on a finite domain with absorbing boundary conditions (Sommerfeld's condition), [\[11\]](#), which correspond to the following Robin-type condition applied on the boundary  $\Gamma$  of the discretization domain  $\Omega$ :

$$-ik(\mathbf{x})u(\mathbf{x}) + \partial_n u(\mathbf{x}) = 0, \quad (4.1)$$

where  $\partial_n u$  denotes the normal derivative of  $u$ . The test sample used below is a homogeneous medium encompassing a circular inclusion of radius 4.5 around the origin with contrast  $f = 1$ . This corresponds to the characteristic function

$$f_a^{\text{disk}}(\mathbf{x}) := \mathbf{1}_{\mathcal{B}_a}(\mathbf{x}), \quad \mathbf{x} \in \mathbb{R}^2, \quad (4.2)$$

of the disk  $\mathcal{B}_a$  with radius  $a > 0$ . The incident plane wave has wave number  $k_0 = 2\pi$  and propagation direction  $\mathbf{s} = (0, -1)^\top$ .

**4.1. Modeling the scattered field assuming incident plane waves.** We consider the solutions  $u^{\text{sca}}$  of [Equation 3.3](#) and  $u^{\text{Born}}$  of [Equation 3.4](#), both satisfying [Equation 4.1](#). As an alternative for computing the Born approximation  $u^{\text{Born}}$ , we discretize the convolution [Equation 3.5](#) with the Green's function  $G$  given in [Equation 3.6](#). In particular, applying an

$N \times N$  quadrature on the uniform grid  $\mathcal{R}_N = \{-r_M, -r_M + 2r_M/N, \dots, r_M - 2r_M/N\}^2$  to Equation 3.5, we obtain

$$u^{\text{Born}}(\mathbf{x}) \approx u_{\text{conv},N}^{\text{Born}}(\mathbf{x}) := \left(\frac{2r_M}{N}\right)^2 \sum_{\mathbf{y} \in \mathcal{R}_N} G(\mathbf{x} - \mathbf{y}) f(\mathbf{y}) e^{ik_0 \mathbf{y} \cdot \mathbf{s}}, \quad \mathbf{x} \in \mathbb{R}^2. \quad (4.3)$$

In Figure 2, we illustrate the solutions. We observe that the transmission waves contain the most energy, that is, waves that “cross” the inclusion. On the other hand, the solution has very low amplitude elsewhere, including the reflected waves. In Figure 2d, we see that the Born approximation leads to an incorrect amplitude of the solution, in particular the imaginary part.

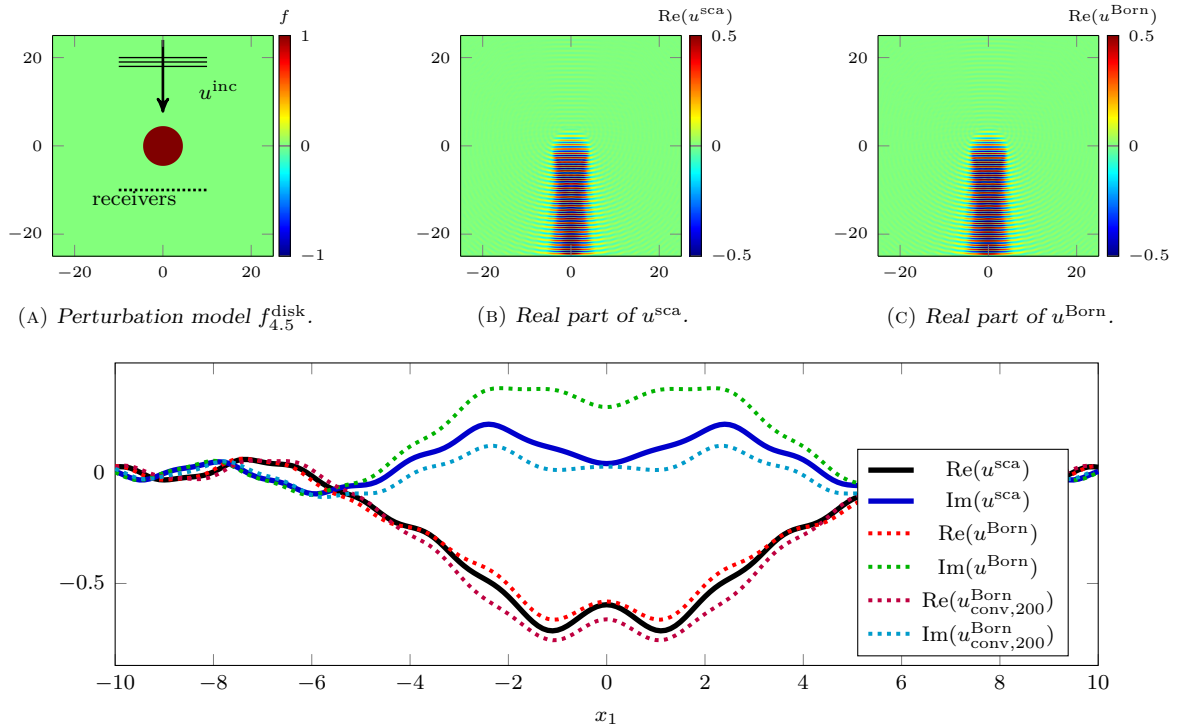


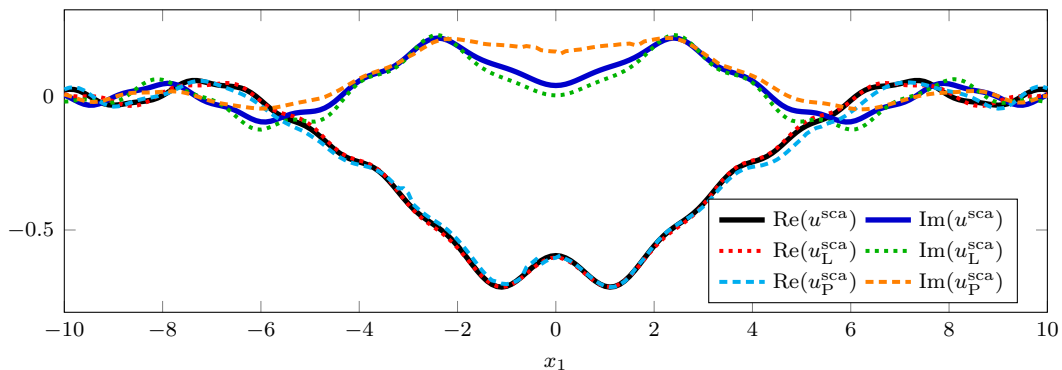
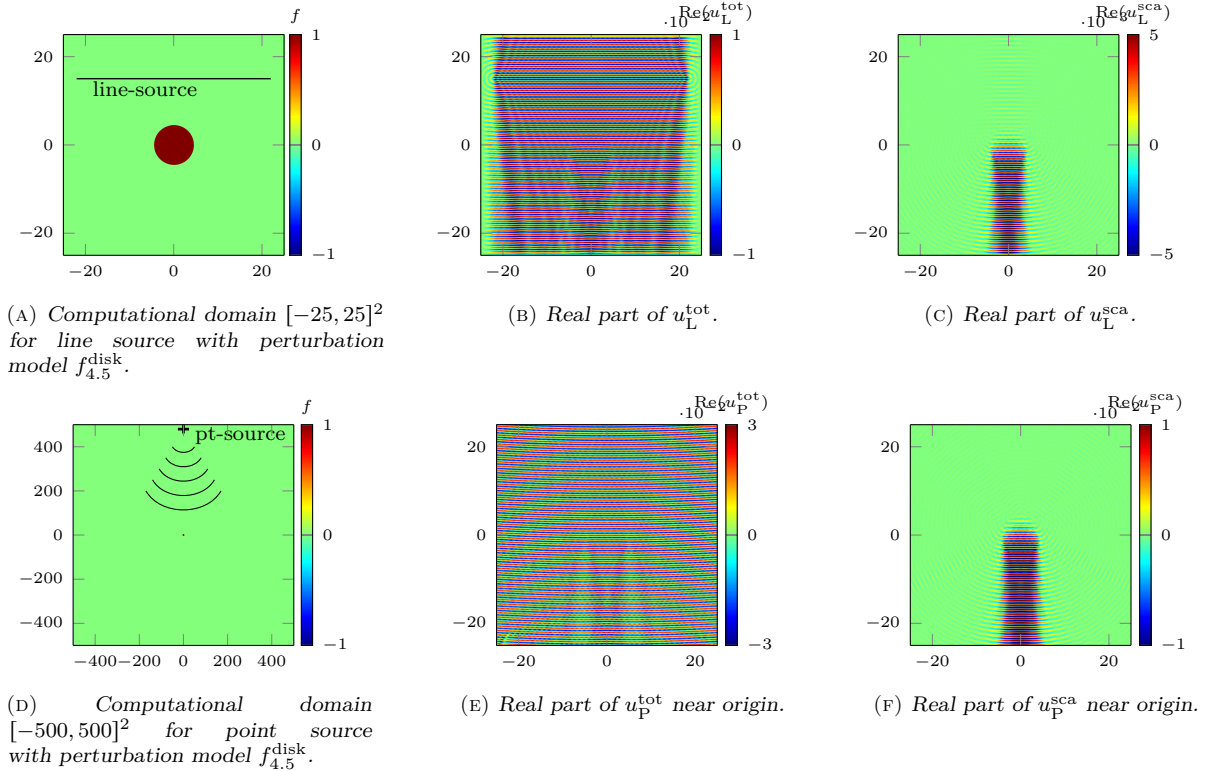
FIGURE 2. Comparison of the scattered wave  $u^{\text{sca}}$  and the Born approximation  $u^{\text{Born}}$ . The computations are performed on a domain  $[-25, 25] \times [-25, 25]$  with boundary conditions given in Equation 4.1. Further, we display  $u_{\text{conv},200}^{\text{Born}}$  which is the Born approximation obtained by the convolution Equation 4.3.

**4.2. Modeling the total field using line and point sources.** The objective is to evaluate how considering line and point sources differs from using incident plane waves, and if the data obtained with both approaches are comparable. To compare the scattered fields obtained from Equation 3.11 and Equation 3.12 with the solution  $u^{\text{sca}}$  of Equation 3.3, one needs to rescale according to

$$u_{\text{P}}^{\text{sca}} = \alpha_{\text{P}} (u_{\text{P}}^{\text{tot}} - u_{\text{P}}^{\text{inc}}), \quad (4.4a)$$

$$u_{\text{L}}^{\text{sca}} = \alpha_{\text{L}} (u_{\text{L}}^{\text{tot}} - u_{\text{L}}^{\text{inc}}), \quad (4.4b)$$

where  $\alpha_{\text{P}}, \alpha_{\text{L}}$  are constants. We illustrate in Figure 3, where the line source is positioned at fixed height  $x_2 = 15$  and composed of 441 points between  $x_1 = -22$  and  $x_1 = 22$ . For the case of a point source, we have to consider a very wide domain, namely  $[-500, 500] \times [-500, 500]$ , and



(g) Comparison of the solutions at fixed height  $x_2 = -10$ .

FIGURE 3. Total field  $u_L^{\text{tot}}$  and scattered field  $u_L^{\text{sca}}$  (line source) and total field  $u_P^{\text{tot}}$  and scattered field  $u_P^{\text{sca}}$  (point source). The line source is composed of  $N_{\text{sim}} = 441$  points at fixed height  $x_2 = 15$ . The computational domain for the point source is very large such that the perturbation is barely visible and the source is positioned in  $\mathbf{x}_0 = (0, 480)^T$ .

the point source is positioned in  $(x_1 = 0, x_2 = 480)$ . In Figure 3g, we plot the corresponding solutions on a line at height  $x_2 = -10$ , i.e., for measurements of transmission waves.

We see that the simulation using the line source is very close to the original solution  $u^{\text{sca}}$ , in fact, it is a more accurate representation than the Born approximation pictured in Figure 2. The simulation using a point source positioned far away is also accurate, except for the middle area of the imaginary part. Furthermore, the major drawback of using a single point source is that it necessitates a very big domain, hence largely increasing the computational cost.

## 5. FOURIER DIFFRACTION THEOREM

In this section we discuss the inverse problem of recovering the scattering potential from measurements of the scattered wave under the Born or Rytov approximations. Before stating the fundamental result in this context, see [Theorem 5.1](#) below, we have to introduce further notation.

We denote by  $\mathcal{F}$  the two-dimensional Fourier transform and by  $\mathcal{F}_1$  the partial Fourier transform with respect to the first coordinate,

$$\begin{aligned}\mathcal{F}\phi(\mathbf{k}) &= (2\pi)^{-1} \int_{\mathbb{R}^2} \phi(\mathbf{x}) e^{-i\mathbf{x}\cdot\mathbf{k}} d\mathbf{x}, & \mathbf{k} \in \mathbb{R}^2, \\ \mathcal{F}_1\phi(k_1, x_2) &= (2\pi)^{-\frac{1}{2}} \int_{\mathbb{R}} \phi(\mathbf{x}) e^{-ik_1x_1} dx_1, & (k_1, x_2) \in \mathbb{R}^2.\end{aligned}$$

For  $k_1 \in [-k_0, k_0]$ , we define

$$\kappa(k_1) := \sqrt{k_0^2 - k_1^2}. \quad (5.1)$$

We can now formulate the Fourier diffraction theorem, see for instance [\[26, Sect. 6.3\]](#), [\[38, Thm. 3.1\]](#) or [\[51\]](#).

**Theorem 5.1** *Let  $f$  be bounded with  $\text{supp } f \subset \mathcal{B}_{r_M}$ . For  $k_1 \in (-k_0, k_0)$ , we have*

$$\mathcal{F}_1 u^{\text{Born}}(k_1, \pm r_M) = \sqrt{2\pi} \frac{ie^{i\kappa r_M}}{2\kappa} \mathcal{F} f \left( (k_1, \pm\kappa)^\top - k_0 \mathbf{s} \right). \quad (5.2)$$

According to the Fourier diffraction theorem, [Theorem 5.1](#), the measurements of the scattered wave  $u$  can be related to the scattering potential  $f$  on a semicircle in  $\mathbf{k}$ -space. Below we discuss how this so-called *k-space coverage* of the experiment is affected by (i) rotating the object and (ii) varying the wave number  $k_0$  of the incident field  $u^{\text{inc}}$ .

**5.1. Rotating the object.** Suppose the object rotates around the origin during the experiment. Then the resulting orientation-dependent scattering potential can be written as

$$f^\alpha(\mathbf{x}) = f(R_\alpha \mathbf{x}), \quad \mathbf{x} \in \mathbb{R}^2,$$

where  $\alpha$  ranges over a (continuous or discrete) set of angles  $A \subset [0, 2\pi]$  and

$$R_\alpha = \begin{pmatrix} \cos \alpha & -\sin \alpha \\ \sin \alpha & \cos \alpha \end{pmatrix} \quad (5.3)$$

is a rotation matrix. If we let  $u^\alpha$  be the Born approximation to the wave scattered by  $f^\alpha$ , the collected measurements are given by

$$u^\alpha(x_1, \pm r_M), \quad x_1 \in \mathbb{R}, \quad \alpha \in A.$$

Exploiting the rotation property of the Fourier transform,  $\mathcal{F}(f \circ R_\alpha) = (\mathcal{F}f) \circ R_\alpha$ , we obtain from [Equation 5.2](#)

$$\mathcal{F}_1 u^\alpha(k_1, \pm r_M) = \sqrt{2\pi} \frac{ie^{i\kappa r_M}}{2\kappa} \mathcal{F} f \left( R_\alpha \left( (k_1, \pm\kappa)^\top - k_0 \mathbf{s} \right) \right). \quad (5.4)$$

Thus the  $\mathbf{k}$ -space coverage, that is, the set of all spatial frequencies at which  $f$  is accessible via the Fourier diffraction theorem, is given by

$$\mathcal{Y} = \left\{ R_\alpha \left( (k_1, \pm\kappa)^\top - k_0 \mathbf{s} \right) \in \mathbb{R}^2 : |k_1| < k_0, \alpha \in A \right\}.$$

It consists of rotated versions (around the origin) of the semicircle  $(k_1, \pm\kappa)^\top - k_0 \mathbf{s}$ , see [Figure 4](#).

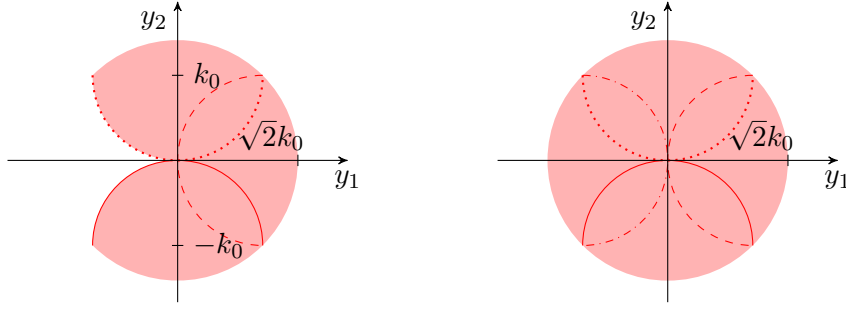


FIGURE 4.  $k$ -space coverage for a rotating object, incidence direction  $\mathbf{s} = (0, 1)$  and measurements taken at  $x_2 = r_M$ . Left: half turn,  $A = [0, \pi]$ . Right: full turn,  $A = [0, 2\pi]$ . The frequency coverage (light red) is a union of infinitely many semicircles, each corresponding to a different orientation of the object. Some of the semicircles are depicted in red: solid arc ( $\alpha = 0$ ), dashed ( $\alpha = \pi/2$ ), dotted ( $\alpha = \pi$ ), dash-dotted ( $\alpha = 3\pi/2$ ).

**5.2. Varying wave number.** Now suppose the object is illuminated or insonified by plane waves with wave numbers ranging over a set  $K \subset (0, +\infty)$ . Recall the definition of the scattering potential  $f_{k_0} = k_0^2(n^2/n_0^2 - 1)$  from Equation 2.2, but note that we have now added a subscript to indicate the dependence of  $f$  on  $k_0$ . If the variation of the object's refractive index  $n$  with  $k_0 \in K$  is negligible, we can write

$$f_{k_0}(\mathbf{x}) = k_0^2 f_1(\mathbf{x}), \quad \mathbf{x} \in \mathbb{R}^2. \quad (5.5)$$

Denoting by  $u_{k_0}$  the Born approximation to the wave scattered by  $f_{k_0}$ , the resulting collection of measurements is

$$u_{k_0}(x_1, \pm r_M), \quad x_1 \in \mathbb{R}, \quad k_0 \in K.$$

Then, according to Equation 5.2, we have

$$\mathcal{F}_1 u_{k_0}(k_1, \pm r_M) = \sqrt{2\pi} \frac{ie^{i\kappa r_M}}{2\kappa} k_0^2 \mathcal{F} f_1((k_1, \pm\kappa)^\top - k_0 \mathbf{s}).$$

Notice that now  $\kappa$  also varies with  $k_0$ . The resulting  $k$ -space coverage

$$\mathcal{Y} = \{(k_1, \pm\kappa)^\top - k_0 \mathbf{s} \in \mathbb{R}^2 : k_0 \in K, |k_1| < k_0\}$$

is a union of semicircles scaled and shifted (in direction of  $-\mathbf{s}$ ) according to  $k_0 \in K$ .

Consider, for example,  $\mathbf{s} = (0, 1)^\top$ , measurements taken at  $x_2 = r_M$  and  $K = [k_{\min}, k_{\max}]$ . Then the  $k$ -space coverage consists of all points  $(y_1, y_2)^\top \in \mathbb{R}^2$  such that  $|y_1| \leq k_{\max}$  and

$$\sqrt{k_{\max}^2 - y_1^2} - k_{\max} \geq y_2 \geq \begin{cases} -|y_1|, & |y_1| \geq k_{\min}, \\ \sqrt{k_{\min}^2 - y_1^2} - k_{\min}, & \text{otherwise,} \end{cases}$$

see Figure 5. Note that, in contrast to the scenarios of Section 5.1, there are large missing parts near the origin.

**5.3. Rotating the object with multiple wave numbers.** We combine the two previous observations by picking a finite number of wave numbers  $K = \{k_0(1), \dots, k_0(n_\omega)\}$  and performing

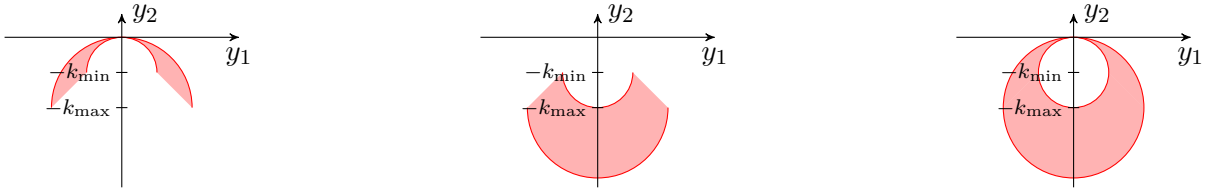


FIGURE 5.  $k$ -space coverage with  $\mathbf{s} = (0, 1)$  where the wave number  $k_0$  covers the interval  $[k_{\min}, k_{\max}]$ . Left: measurements taken at  $x_2 = r_M$ . Center: measurements taken at  $x_2 = -r_M$ . Right: both measurements combined.

a full rotation of the object for each  $k_0(j)$ . Let  $u_{k_0(j)}^\alpha$  be the Born approximation to the wave scattered by  $f_{k_0(j)}^\alpha = k_0(j)^2 f_1 \circ R_\alpha$ . Then the full set of measurements is given by

$$u_{k_0(j)}^\alpha(x_1, \pm r_M), \quad x_1 \in \mathbb{R}, \quad \alpha \in [0, 2\pi], \quad 1 \leq j \leq n_\omega, \quad (5.6)$$

and the Fourier diffraction theorem yields

$$\mathcal{F}_1 u_{k_0(j)}^\alpha(k_1, \pm r_M) = \sqrt{2\pi} \frac{i e^{i\kappa r_M}}{2\kappa} k_0(j)^2 \mathcal{F} f_1 (R_\alpha((k_1, \pm \kappa)^\top - k_0(j)\mathbf{s})). \quad (5.7)$$

We deduce from [Section 5.1](#) and [Section 5.2](#) that the resulting  $k$ -space coverage  $\mathcal{Y}$  is the union of disks with radii  $\sqrt{2}k_0(j)$ , all centered at the origin. Hence,  $\mathcal{Y}$  is just the largest disk, that is, the one corresponding to the largest wave number  $\max_j k_0(j)$ . However, smaller disks in  $k$ -space are covered more often, which might improve reliability of the reconstruction for noisy data.

## 6. RECONSTRUCTION METHODS

In the following, we assume data generated by line-sources according to the setup described in [Section 4.2](#). Therefore, our initial data consist in total field simulated measurements.

**6.1. Reconstruction using Full Waveform Inversion.** For the identification of the physical properties of the medium, the *Full Waveform Inversion* (FWI) relies on an iterative minimization of a misfit functional which evaluates a distance between numerical simulation and measurements of the total field, i.e., we do not make assumptions on the fields and background perturbation. The Full Waveform Inversion method arises in the context of seismic inversion for sub-surface Earth imaging, cf. [\[2, 33, 48, 43, 50\]](#), where the measured seismograms are compared to simulated waves.

Let us first recall the definition of the wave number  $k$ , which can be separated into the angular frequency  $\omega$  and wave-speed  $c$  such that

$$k(\mathbf{x}) = \frac{\omega}{c(\mathbf{x})} = \frac{2\pi\nu}{c(\mathbf{x})}, \quad (6.1)$$

with  $\nu$  the ordinary frequency. The wave number  $k$  is further decomposed into a background part  $k_0$  and a perturbation  $f$ , see [Equation 2.2](#), such that  $k^2 = k_0^2 + f$ . Therefore, the relation between  $f$  and the (frequency independent) wave-speed  $c$  is given by

$$c(\mathbf{x}) = \sqrt{\frac{(\omega c_0)^2}{\omega^2 + f(\mathbf{x}) c_0^2}}, \quad (6.2)$$

where  $c_0$  is the background wave-speed, which shall be used as an initial model.

Given some measurements  $\mathbf{d}$  of the total field, the quantitative reconstruction of the wave-speed  $c$  is performed following the minimization of the misfit functional  $\mathcal{J}$  such that

$$\min_c \mathcal{J}(c), \quad \mathcal{J} = \text{dist}(\mathcal{R}u, \mathbf{d}), \quad \text{where } u \text{ solves Equation 3.12.} \quad (6.3)$$

Here,  $\text{dist}(\cdot)$  is a distance function to evaluate the difference between the measurements and the simulations, and  $\mathcal{R}$  is a linear operator to restrict the solution to the positions of the receivers. For simplicity, we do not encode a regularization term in Equation 6.3 and refer the readers to, e.g., [19, 27] and the reference therein.

Several formulations of the distance function have been studied for FWI (in particular for seismic applications), such as a logarithmic criterion, [45], the use of the signal's phase or amplitude, [4, 44], the use of the envelope of the signal, [20], criteria based upon crosscorrelation, [34, 49, 15, 17], or optimal transport distance, [35]. Here, we rely on a least-squares approach where the misfit functional is defined as the  $L^2$  distance between the data and simulations:

$$\mathcal{J}(c) := \frac{1}{2} \sum_{\omega} \sum_j \|\mathcal{R}u(c, \omega, s_j) - \mathbf{d}(\omega, s_j)\|_2^2, \quad (6.4)$$

where the index  $j$  refers to the different sources in the acquisition. We have encoded a sum over the frequency  $\omega$ , which are chosen in accordance with the frequency content available in measurements. In the computational experiments, we further investigate uni- and multi-frequency reconstructions.

The minimization of the misfit functional Equation 6.4 follows an iterative Newton-type method as depicted in Algorithm 1. Due to the computational cost, we use first-order information and avoid the Hessian computation, [50]: Namely, we rely on the nonlinear conjugate gradient method for the model update, cf. [39, 13]. Furthermore, to avoid the formation of the dense Jacobian, the gradient of the misfit functional is computed using the adjoint-state method, cf. [43, 40, 3, 18]. In Algorithm 1, we further implement a progression in the frequency content, which is common to mitigate the ill-posedness of the nonlinear inverse problem, [5]. We further invert each frequency independently, from low to high, as advocated by [3, 16]. For the implementation details using the HDG discretization, we refer to [18].

```

Starting from an initial wave-speed model  $c_0$ .
for frequency  $\omega_i = \omega_1, \dots, \omega_{n_\omega}$  do
  for iteration  $j = 1, \dots, n_{iter}$  do
    Set global iteration number  $l := (i - 1)n_{iter} + j$ ;
    Solve Equation 3.12 using current wave-speed model  $c_l$  and frequency  $\omega_j$  (i.e.,
       $k = \omega_j/c_l$ );
    Evaluate the misfit functional Equation 6.4;
    Compute the gradient of the misfit functional using the adjoint-state method;
    Update the wave-speed model using nonlinear conjugate gradient method to
      obtain  $c_{l+1}$ .
  end
end

```

**Algorithm 1:** Iterative reconstruction of the wave-speed model following the minimization of the misfit functional. At each iteration, the total field solution to Equation 3.12 is computed and the gradient of the misfit functional is used to update the wave-speed model. The algorithm stops when the prescribed number of iterations is performed for all of the frequencies of interest.

**Remark 6.1** In our computational experiments, we apply FWI without any a-priori information regarding the model representation. Namely, we start from the total field data, which are solutions to [Equation 3.12](#), and invert with respect to the (frequency independent) wave speed  $c$  defined in [Equation 6.2](#). We could instead incorporate its specific representation as it is decomposed into a (known) smooth background and the perturbation (following relation  $k^2 = k_0^2 + f$ ). Then, FWI could certainly be improved if reformulated with such a model decomposition, which corresponds to the data-space reflectivity inversion of [\[7, 16\]](#).

**6.2. Reconstruction based on the Born approximation.** In this section, we present numerical methods for the computation of the Born and Rytov approximations from [Equation 3.4](#) and [Equation 3.9](#), respectively, as well as the reconstruction of the scattering potential. We concentrate on the case of full rotations of the object using incident waves with different wave numbers  $k_0(j)$ , see [Section 5.3](#). The tomographic reconstruction is based on the Fourier diffraction theorem, [Theorem 5.1](#).

In the following, we describe the discretization steps we apply. For  $N \in 2\mathbb{N}$ , let

$$\mathcal{I}_N := \left\{ -\frac{N}{2} + j : j = 0, \dots, N-1 \right\}.$$

We sample the scattering potential  $f$  on the uniform grid  $\mathcal{R}_N := \frac{2r_s}{N} \mathcal{I}_N^2$  in the square  $[-r_s, r_s]^2$  for some  $r_s > 0$ . We assume that we are given measurements of the Born approximation

$$u_{k_0(j)}^\alpha(x_1, \pm r_M), \quad x_1 \in [-l_M, l_M],$$

for  $\alpha \in A \subset [0, 2\pi]$  and  $j \in \{1, \dots, n_\omega\}$ , cf. [Equation 5.6](#). We want to reconstruct the scattering potential  $f_1$ , recall [Equation 5.5](#), utilizing [Equation 5.7](#). We adapt the reconstruction approach of [\[30\]](#), which is written for the 3D case. First, we need to approximate the partial Fourier transform

$$\mathcal{F}_1 u_{k_0(j)}^\alpha(k_1, \pm r_M) = (2\pi)^{-\frac{1}{2}} \int_{\mathbb{R}} u_{k_0(j)}^\alpha(x_1, \pm r_M) e^{-ix_1 k_1} dx_1, \quad k_1 \in [-k_0, k_0]. \quad (6.5)$$

The *discrete Fourier transform* (DFT) of  $u(\cdot, \pm r_M)$  on  $m$  equispaced points  $x_1 \in (2l_M/m)\mathcal{I}_m$  can be defined by

$$\mathbf{F}_{1,m} u(k_1, \pm r_M) := \frac{1}{\sqrt{2\pi}} \frac{2l_M}{m} \sum_{x_1 \in \frac{2l_M}{m} \mathcal{I}_m} u(x_1, \pm r_M) e^{-ix_1 k_1}, \quad k_1 \in \frac{\pi}{l_M} \mathcal{I}_m, \quad (6.6)$$

which gives an approximation of [Equation 6.5](#). Then [Equation 5.7](#) yields

$$k_0(j)^2 \mathcal{F} f_1(R_\alpha((k_1, \pm \kappa)^\top - k_0(j)\mathbf{s})) = -i \sqrt{\frac{2}{\pi}} \kappa e^{-i\kappa r_M} \mathcal{F}_1 u_{k_0(j)}^\alpha(k_1, \pm r_M) \quad (6.7)$$

for  $|k_1| \leq k_0(j)$ . Considering that we sample the angle  $\alpha$  on the equispaced, discrete grid  $A = (2\pi/n_A)\{0, 1, \dots, n_A - 1\}$ , [Equation 6.6](#) provides an approximation of  $\mathcal{F}f$  on the non-uniform grid

$$\mathcal{Y}_{m,n_A} := \left\{ R_\alpha((k_1, \pm \kappa)^\top - k_0(j)\mathbf{s}) : \right. \\ \left. k_1 \in \frac{\pi}{l_M} \mathcal{I}_m, |k_1| \leq k_0(j), \alpha \in \frac{2\pi}{n_A} \{0, 1, \dots, n_A - 1\}, j = 1, \dots, n_\omega \right\}$$

in k-space, from which we want to reconstruct the scattering potential  $f$ .

Let  $M$  be the cardinality of  $\mathcal{Y}_{m,n_A}$ . The two-dimensional *nonuniform discrete Fourier transform* (NDFT) is the linear operator  $\mathbf{F}_N: \mathbb{R}^{N^2} \rightarrow \mathbb{R}^M$  defined for the vector  $\mathbf{f}_N := (f(\mathbf{x}))_{\mathbf{x} \in \mathcal{R}_N}$  elementwise by

$$\mathbf{F}_N \mathbf{f}_N(\mathbf{y}) := \frac{1}{2\pi} \frac{(2r_s)^2}{N^2} \sum_{\mathbf{x} \in \mathcal{R}_N} f(\mathbf{x}) e^{-i\mathbf{x} \cdot \mathbf{y}}, \quad \mathbf{y} \in \mathcal{Y}_{m,n_A}, \quad (6.8)$$

see [41, Section 7.1]. It provides an approximation of the Fourier transform

$$\mathcal{F}f(\mathbf{y}) \approx \mathbf{F}_N \mathbf{f}_N(\mathbf{y}), \quad \mathbf{y} \in \mathcal{Y}_{m,n_A}.$$

Solving an equation  $\mathbf{F}_N \mathbf{f}_N(\mathbf{y}) = \mathbf{b}$  for  $\mathbf{f}_N$  amounts to applying an *inverse NDFT*, which usually utilizes an iterative method such as the conjugate gradient method on the normal equations (CGNE), see [32] and [41, Section 7.6]. One should be aware that the notation regarding conjugate gradient algorithms varies in the literature: the algorithm called CGNE in [21], is known as CGNR in [32]. Conversely, the algorithm CGME in [21] is known as CGNE in [32].

In conclusion, our method for computing  $f$  given the Born approximation  $u^{\text{Born}}$  is summarized in [Algorithm 2](#).

Starting from measurement data

$$u_{k_0(j)}^\alpha(x_1, r_M), \quad x_1 \in \frac{2l_M}{m} \mathcal{I}_m, \quad \alpha \in \frac{2\pi}{n_A} \{0, \dots, n_A - 1\}, \quad j = 1, \dots, n_\omega.$$

**for**  $j = 1, \dots, n_\omega$  **do**

    | Compute  $-i\sqrt{\frac{2}{\pi}} \kappa e^{-i\kappa r_M} \mathbf{F}_{1,m} u_{k_0(j)}^\alpha(k_1, \pm r_M)$ , with a DFT in [Equation 6.6](#)

**end**

    Solve [Equation 6.7](#) for  $f$  with the conjugate gradient method

**Algorithm 2:** Iterative reconstruction of the scattering potential  $f$  based on the Born approximation using an inverse NDFT.

The Rytov approximation  $u^{\text{Rytov}}$ , see [Equation 3.9](#), is closely related to the Born approximation, but it has a different physical interpretation. Assuming that the measurements arise from the Rytov approximation, we apply [Equation 3.10](#) to obtain  $u^{\text{Born}}$  from which we can proceed to recover  $f$  as shown above. We note that the actual implementation of [Equation 3.10](#) requires a phase unwrapping because the complex logarithm is unique only up to adding  $2\pi i$ , cf. [37]. In particular, we use in the two-dimensional case

$$u^{\text{Born}} = u^{\text{inc}} \left( i \text{unwrap} \left( \arg \left( \frac{u^{\text{Rytov}}}{u^{\text{inc}}} + 1 \right) \right) + \ln \left| \frac{u^{\text{Rytov}}}{u^{\text{inc}}} + 1 \right| \right), \quad (6.9)$$

where  $\arg$  denotes the principle argument of a complex number and  $\text{unwrap}$  denotes a standard unwrapping algorithm. For the reconstruction with the Rytov approximation, we can use [Algorithm 2](#) as well, but we have to preprocess the data  $u$  by [Equation 6.9](#).

## 7. NUMERICAL EXPERIMENTS

In this section, we carry out numerical experiments comparing the reconstruction obtained with FWI ([Section 6.1](#)) and Born and Rytov approximations ([Section 6.2](#)), using single and multi-frequency data-sets. We consider different media with varying shapes and amplitude for the embedded objects. The measurement data of  $u$  is computed “in silico” using the total field

obtained from line-sources, as described in [Section 4.2](#). Furthermore, we incorporate white Gaussian noise in the simulated data, with a signal-to-noise ratio of 50 dB. In addition, for the inversion experiments with FWI which use the same software as the data generation ([hawen](#), see [\[14\]](#) and [footnote 1](#)), the computational setup for modeling and inversion use different discretization mesh and order of polynomials.

We perform a full rotation of the object for a single or for multiple frequencies  $\nu$  and thus wave numbers  $k_0 = 2\pi\nu$ , cf. [Section 5.3](#). For different frequencies, the scattering potential is scaled according to [Equation 5.5](#). We always reconstruct the rescaled scattering potential  $f_1$ , which we will simply denote by  $f$  in the following.

We compare the reconstruction quality based on the *peak signal-to-noise ratio* (PSNR) of the reconstruction  $\mathbf{g}$  with respect to the ground truth  $\mathbf{f}$  determined by

$$\text{PSNR}(\mathbf{f}, \mathbf{g}) := 10 \log_{10} \frac{\max_{\mathbf{x} \in \mathcal{R}_N} |\mathbf{f}(\mathbf{x})|^2}{N^{-2} \sum_{\mathbf{x} \in \mathcal{R}_N} |\mathbf{f}(\mathbf{x}) - \mathbf{g}(\mathbf{x})|^2}, \quad (7.1)$$

where higher values indicate a better reconstruction quality. It appears reasonable to take as ground truth the pixel values as the averages of their three-point neighborhood on a finer grid,

$$\mathbf{f}_N^{\text{av}}(\mathbf{x}) := \frac{1}{3^2} \sum_{\mathbf{j} \in \{-1,0,1\}^2} f\left(\mathbf{x} + \frac{2r_s}{3N}\mathbf{j}\right), \quad \mathbf{x} \in \mathcal{R}_N.$$

**7.1. Reconstruction of circular contrast with various amplitudes and sizes.** For these initial reconstruction experiments, we consider a circular inclusion in a constant background wave-speed, namely the scattering potential of [Equation 4.2](#). We investigate different sizes and contrasts for the object, as shown in [Figure 6](#). The data are generated for 40 angles of incidence equally partitioned between  $0^\circ$  to  $351^\circ$ , every  $9^\circ$ . Let us note that in this context of a circularly symmetric inclusion, the data of each angle are similar and correspond to that of [Figure 3](#) for  $f_{4.5}^{\text{disk}}$ .

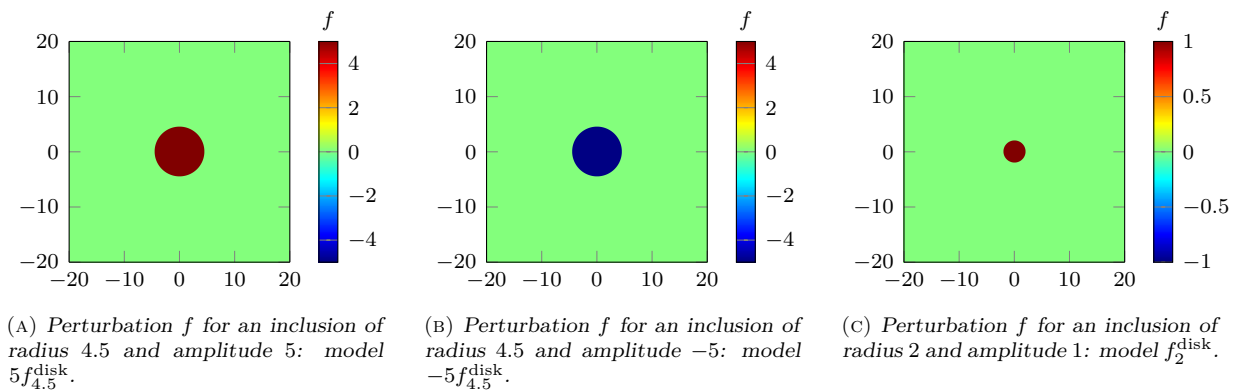


FIGURE 6. Different perturbation models  $f$  used for the computational experiments, given for frequency  $\nu = \omega/(2\pi) = 1$ , with the relation to the wave-speed given in [Equation 6.2](#). Both the size and contrast of the inclusion vary: we consider two radii (4.5 and 2) and three contrasts  $f = 1$ ,  $f = 5$  and  $f = -5$  (the corresponding wave-speed is  $c = 0.9876$ ,  $c = 0.9421$  and  $c = 1.0701$  respectively), for a total of six configurations. The computations are carried out on a domain  $[-50, 50] \times [-50, 50]$ , i.e., in a slightly larger setup than [Figure 3](#), and we only picture the area near the origin for clearer visualization.

**7.1.1. Reconstruction using FWI with single-frequency data-sets.** We first only use data at frequency  $\nu = \omega/(2\pi) = 1$  for the reconstruction of the different perturbations illustrated in Figure 6. With the background  $k_0 = 2\pi$  (i.e., wave-speed of 1), it means that we only rely on waves which have a wavelength of size 1 when propagating in the (homogeneous) background. In the case of a single frequency, only the inner loop remains in Algorithm 1, and we perform 50 iterations. In Figure 7, we picture the reconstruction obtained for the six different perturbations  $f$ . We observe that the reconstruction of the smaller inclusion of radius 2 (Figures 7a, 7b and 7c) is accurate, both in terms of the circular shape, and in terms of amplitude. In the case of the larger inclusion of radius 4.5, the mild amplitude (Figure 7d) is accurately recovered, while the stronger contrasts (Figures 7e and 7f) are only partially retrieved. Here, the outer disk of the inclusion appears, but the amplitude is incorrect with a ring effect, and incorrect values in the inner area. Therefore, the reconstruction using single-frequency data is limited and its success depends on two factors: the size of the inclusion and its contrast.

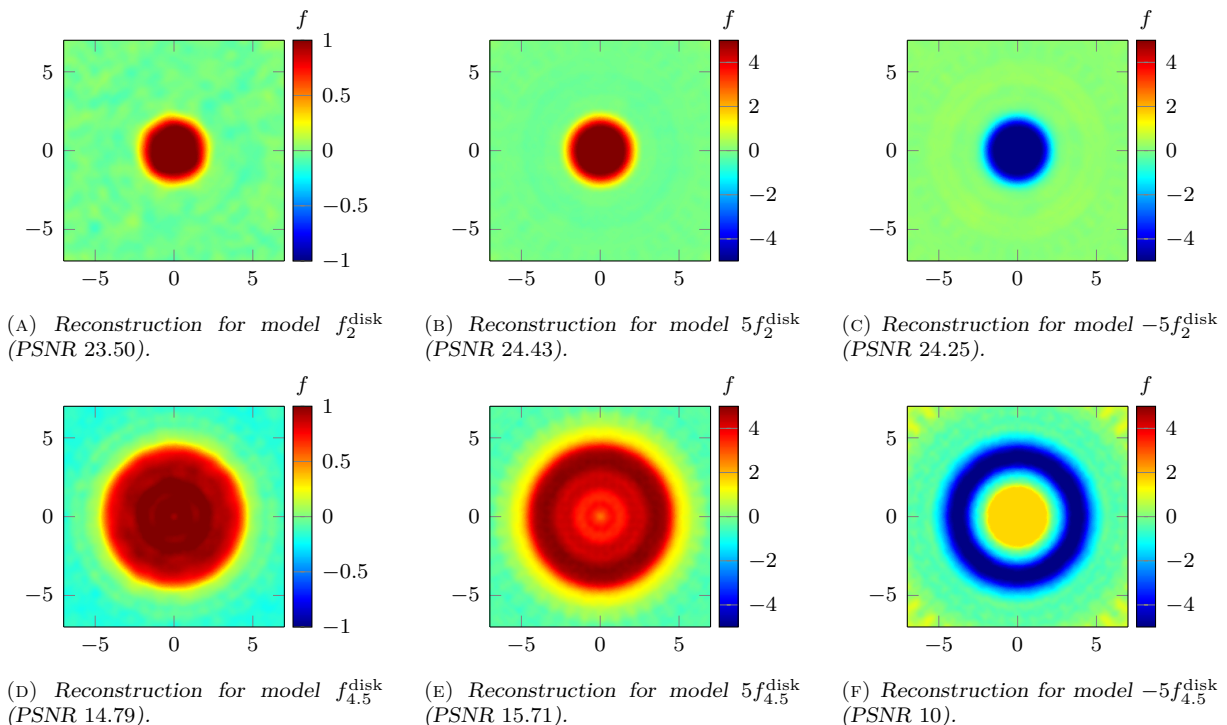


FIGURE 7. Reconstruction using iterative minimization using data of frequency  $\nu = 1$  only. In each cases, 50 iterations are performed and the initial model consists in a constant background where  $k_0 = 2\pi$ . The data consist of 40 different angles of incidence from  $0^\circ$  to  $351^\circ$ .

**7.1.2. Reconstruction using FWI with multiple frequency data-sets.** The difficulty of recovering a large inclusion with a strong contrast can be mitigated by the use of multi-frequency data-sets, allowing a multi-scale reconstruction [5, 16]. We now carry out the iterative reconstruction using increasing frequencies, starting with  $\nu = 0.2$  and up to  $\nu = 1$ . Following [16], we use a sequential progression, that is, every frequency is inverted separately. The reconstructions for the inclusion of radius 4.5 and contrast  $f = \pm 5$  are pictured in Figure 8. Contrary to the case where only one frequency is used (see Figure 7d), the reconstruction is now very accurate and stable: the amplitude of the contrast is accurately retrieved and the circular shape is clear, avoiding the circular artifacts observed in Figures 7e and 7f.

**Remark 7.1** It is possible to recover the model with a single frequency, that needs to be carefully chosen depending on the size of the object and the amplitude of the contrast. We have seen in

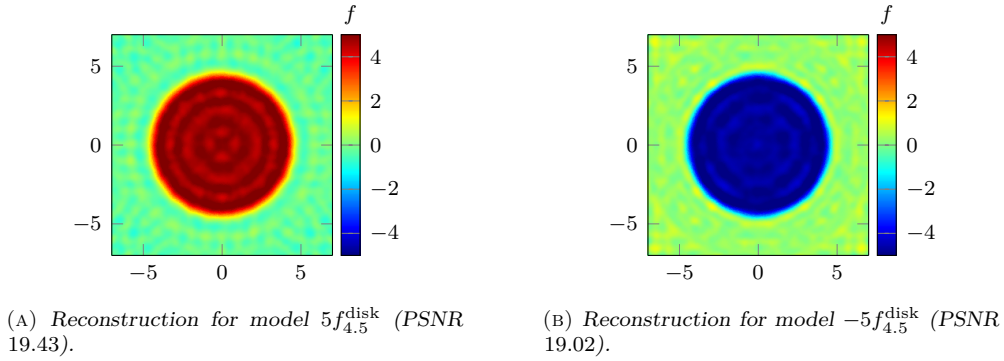


FIGURE 8. Reconstruction using multi-frequency data from  $\nu = 0.2$  to  $\nu = 1$ . The initial model consists in a constant wave-speed  $c_0 = 1$ . The data consist of 40 different angles of incidence from  $0^\circ$  to  $351^\circ$ .

Figure 7 that the frequency  $\nu = 1$  is sufficient for the inclusion of radius 2 but for the inclusion of radius 4.5, we need a lower frequency (i.e., larger wavelength) to uncover the (larger) inclusion. We illustrate in Figure 9 the reconstruction using data at only  $\nu = 0.7$ , where we see that the shape and contrast are retrieved accurately. Nonetheless, it is hard to predict this frequency a-priori and we believe it remains more natural to use multiple frequencies (when available in the data), to ensure the robustness of the algorithm.

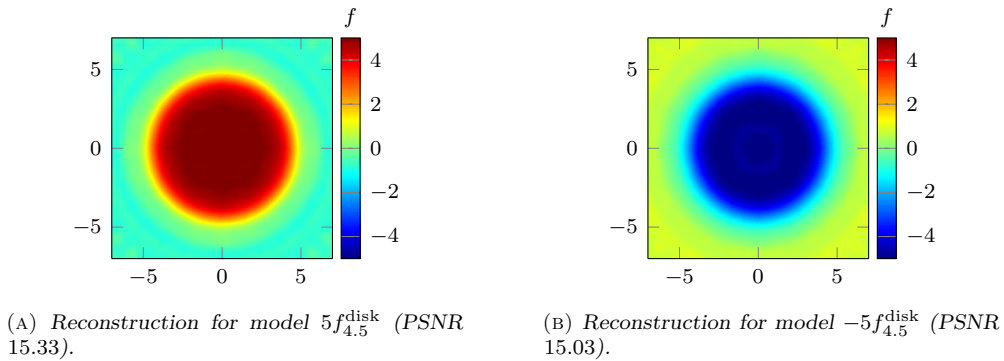


FIGURE 9. Reconstruction using frequency  $\nu = 0.7$ . The initial model consists in a constant wave-speed  $c_0 = 1$ . The data consist of 40 different angles of incidence from  $0^\circ$  to  $351^\circ$ .

**7.1.3. Reconstruction using Born and Rytov approximations.** For the reconstruction with Algorithm 2, which relies on the Born or Rytov approximation, we use the same data as in the above experiment generated with the forward model of line sources in subsection 3.2.2. We have the data  $u_{k_0}^\alpha(r_1, r_M)$  on the 200 point uniform grid  $x_1 \in 10^{-1} \mathcal{I}_{200} \subset [-l_M, l_M]$  with  $l_M = 10$ , and  $n_A = 40$  angles of incidence. We use the grid size  $N = 240$  and the radius  $r_s = N/(8\sqrt{2}) \approx 10$ . The tests indicate that  $r_s$  should not be smaller than  $l_M$ . Since we have  $k_1^2 \leq k_0^2$  and the distance between to grid points of  $k_1$  is  $\pi/l_M$ , only around  $2k_0 l_M/\pi \approx 40$  of them contribute to the data of the inverse NDFT.

In the following tests, we use a fixed number of 20 iteration steps in the conjugate gradient method. Initially, we use the frequency  $\nu = 1$  of the incident wave, therefore  $k_0 = 2\pi$  and the wavelength is  $\lambda = 1$ , such that all measurements in  $\mathbf{x}$  are in multiples of the wavelength. Reconstructions of the circular function  $f_a^{\text{disk}}$  from Equation 4.2 are shown in Figure 10. We note that all reconstructions are reasonably good, where the Rytov reconstruction looks slightly better inside the object.

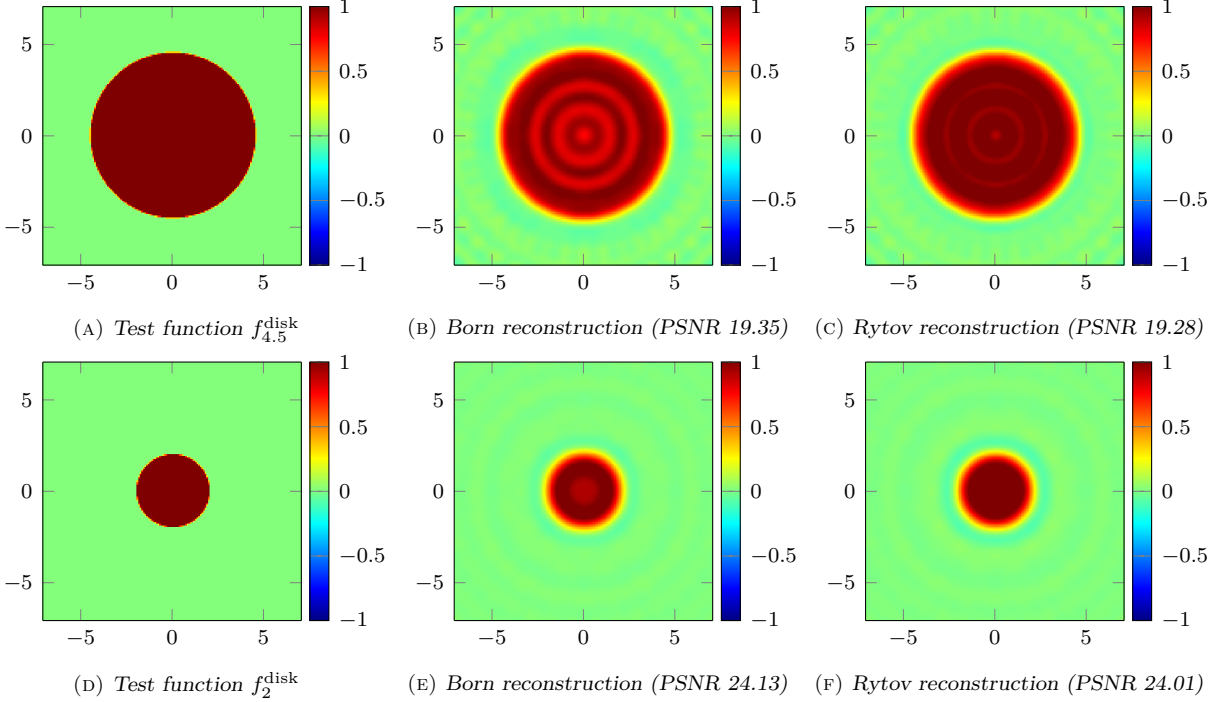


FIGURE 10. Reconstructions with with the Born and Rytov approximation, where the data  $u(\cdot, r_M)$  is generated with the full waveform model. The incident field has the frequency  $\nu = 1$ . Visible is only the cut out center, where we compute the PSNR.

For a higher amplitude of the test function, the limitations of the linear models become apparent. In Figure 11, we see that the Born reconstruction of the larger object fails, and for the smaller object only the Rytov approximation yields a good reconstruction, which is consistent with Remark 3.1. With the Born approximation, we recognize the object’s shape but not its amplitude, which is consistent with the observations in [36]. However, as we see in Figure 7, even the FWI reconstruction makes a considerable error in the object’s interior, and we cannot expect the linear models to be better.

In Figure 12, we use the same setup as before, but with the frequency  $\nu = 0.7$  instead of  $\nu = 1$  and thus the wave number  $k_0 = 2\pi\nu$ . Apparently, the reconstruction becomes worse with lower frequency, because it provides a smaller k-space coverage. We note that the image shows the scattering potential  $f$  scaled for frequency  $\nu = 1$ .

**7.2. Reconstruction of embedded shapes.** We consider a more challenging scenario with shapes embedded in the background medium. In Figure 13a, we picture the perturbation  $f$  consisting of a disk and heart included in an ellipse-shaped contrast, with  $f$  varying from 0 to 0.5. The computational domain corresponds to an interval  $[-20, 20] \times [-20, 20]$ , with line-sources positioned at a distance  $R = 10$  and receivers in  $r_M = 6$  to capture the data. The data are generated using 100 incidence angles, following the steps described in Section 4.2, and we illustrate in Figure 13 for the source of angle of incidence  $-90^\circ$ .

**7.2.1. Reconstruction using FWI.** We carry out the reconstruction following Algorithm 1, and the results are pictured in Figure 14, where we compare the use of single and multi-frequency data. In this example, we see that with relatively low frequency data (i.e., relatively large wavelength), such as for frequency  $\nu = 0.7$  and  $\nu = 1$ , the reconstruction is smooth,

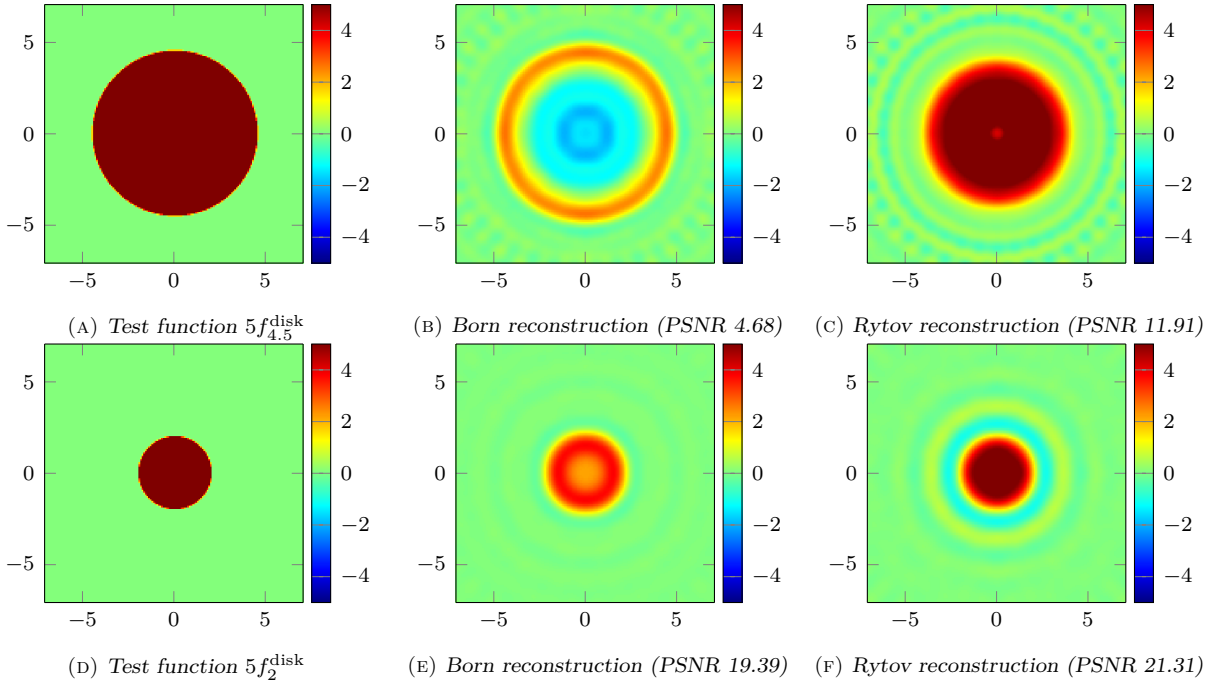


FIGURE 11. Same setting as in Figure 10, but with a higher amplitude of 5.

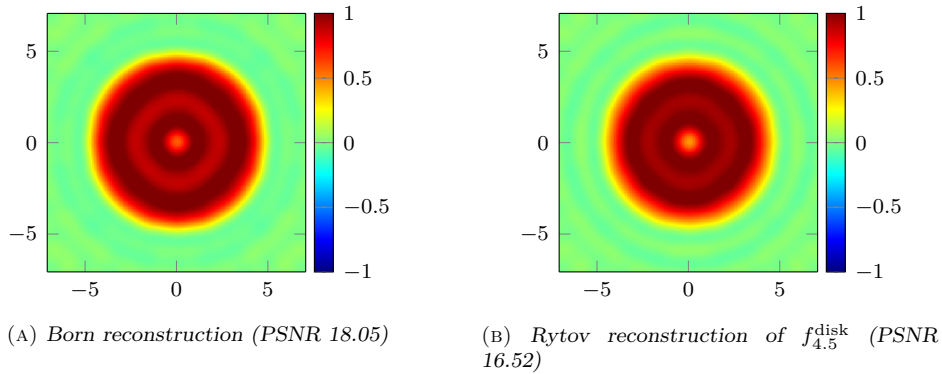


FIGURE 12. Reconstructions of  $f_{4.5}^{\text{disk}}$ , where the incident field has the frequency  $\nu = 0.7$  instead of 1. The rest of the setting is from Figure 10.

see Figure 14a and Figure 14b, and one needs to use smaller wavelengths to obtain a better reconstruction, see Figure 14c and Figure 14d. In Figure 14e, we see that multi-frequency data gives the best reconstruction, it is also the most robust as one does not need to anticipate the appropriate wavelength before carrying out the reconstruction. Here both the shapes and contrast in amplitude are accurately obtained. We notice some oscillatory noise in the reconstructed models, which could certainly be reduced by incorporating a regularization criterion in the minimization ([19]).

In Figure 15, we conduct a similar computational experiment, but increasing the contrast in the included heart shape where  $f$  has now a value of 2, see Figure 15a. We provide single and multi-frequency reconstructions, and observe that large wavelengths still provide a smooth reconstruction. The high contrast in the heart is well recovered.

**7.2.2. Reconstruction using Born and Rytov approximations.** We perform the reconstruction with Algorithm 2 of the test function from Figure 13, from the same simulated data

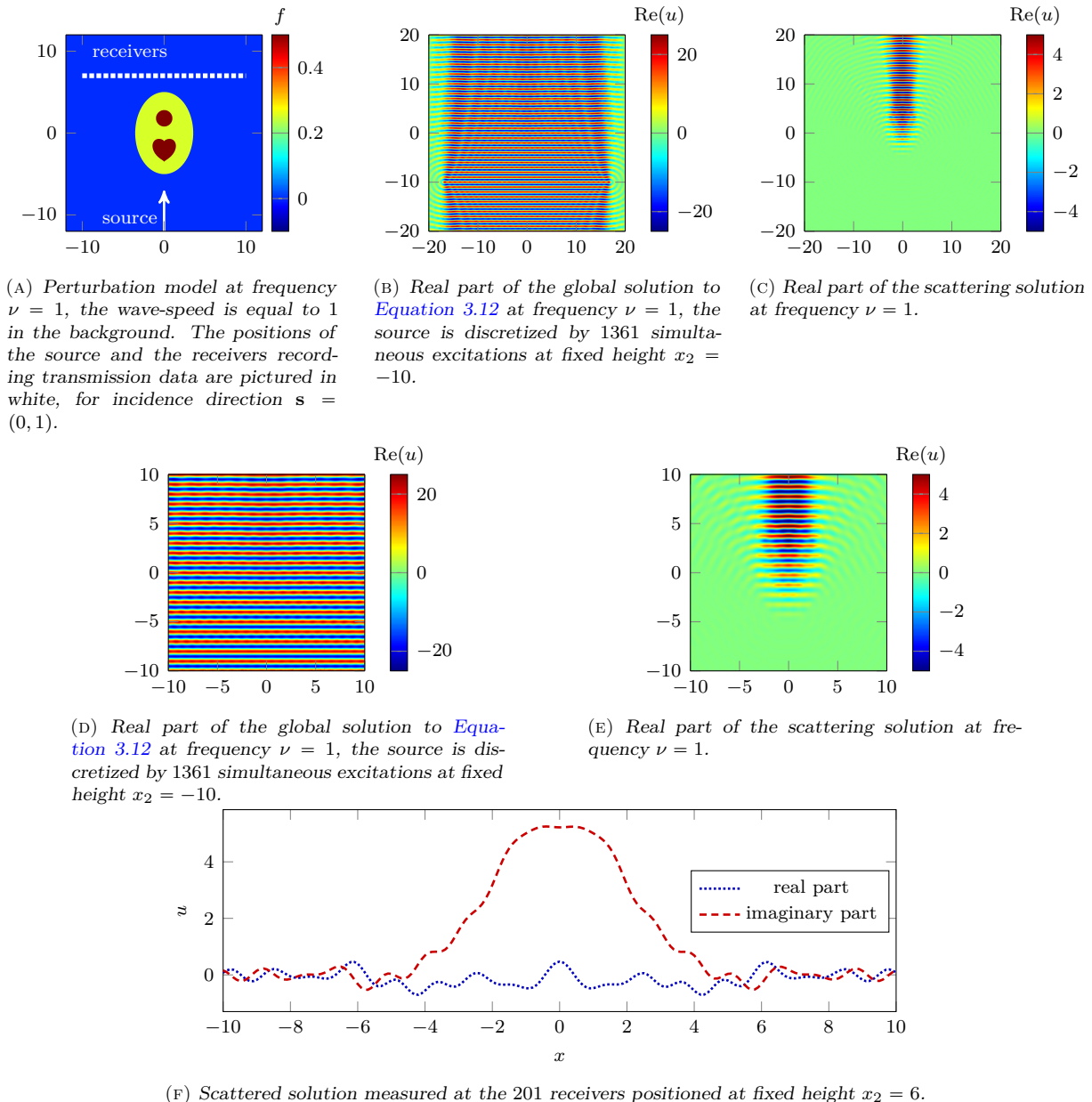


FIGURE 13. Illustration of the acquisition setup and generated data. The computations are carried out on a domain of size  $[-20, 20] \times [-20, 20]$ . While FWI uses the total field, the reconstruction based upon Born and Rytov approximations use the scattered solutions, obtained after removing a reference solution corresponding to a propagation in an homogeneous medium, cf. Section 3.

as in subsection 7.2.1. In the following tests, we discretize  $f$  on a finer grid of resolution  $N = 720$ , which covers the same radius  $r_s = 15/\sqrt{2}$  as in the previous subsection. Our data consists of  $n_A = 100$  rotations, with the rotation angle  $\alpha$  equispaced on  $[0, 2\pi]$ , see Equation 5.3. The PSNR is computed only on the central part of the grid that is visible in the image. Since we know that the  $f$  is real-valued, we take only the real part of the reconstruction. We have added a small amount of white Gaussian noise to the data, with a relative amplitude of  $-50$  dB, from the Matlab routine `awgn`. For simplicity, we use a constant number of 12 iterations in the conjugate gradient method of the inverse NDFT.

The Born and Rytov reconstructions are shown in Figure 16, where the data  $u$  is the same as in subsection 7.2.1. The reconstruction with a higher frequency  $\nu$  of the incident wave is more

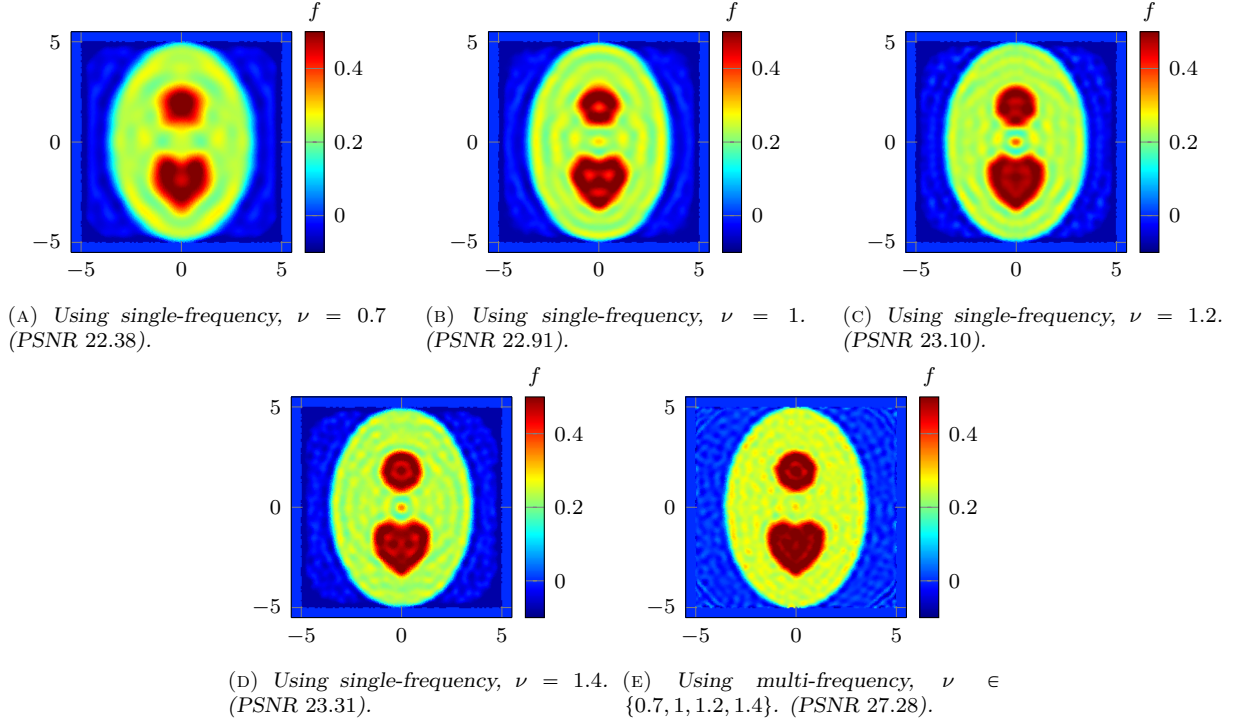


FIGURE 14. Reconstruction of the model [Figure 13a](#) with FWI and starting from a homogeneous background with  $f = 0$ . The models are given at frequency  $\nu = 1$  and the wave-speed is equal to 1 in the background.

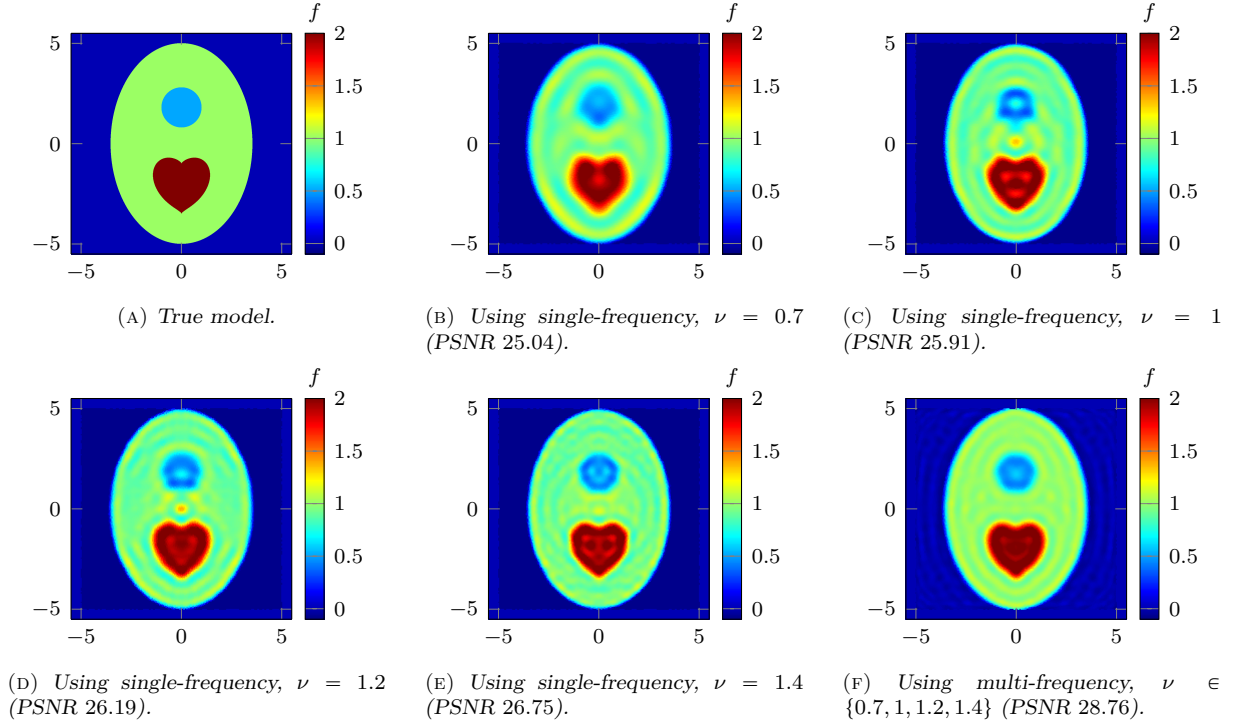


FIGURE 15. Reconstruction with FWI starting from a homogeneous background with  $f = 0$ . The models are given at frequency  $\nu = 1$  and the wave-speed is equal to 1 in the background.

accurate, since it provides a larger frequency coverage, which is the disk of radius  $\sqrt{2}k_0 = \sqrt{8}\pi\nu$ , see [Section 5](#). Moreover, the multi-frequency reconstruction is shown in [Figure 16](#) (G) and (H).

Even though the multi-frequency setup covers the same disk in Fourier space, it still seems superior because we have more data points of the Fourier transform  $\mathcal{F}f$ .

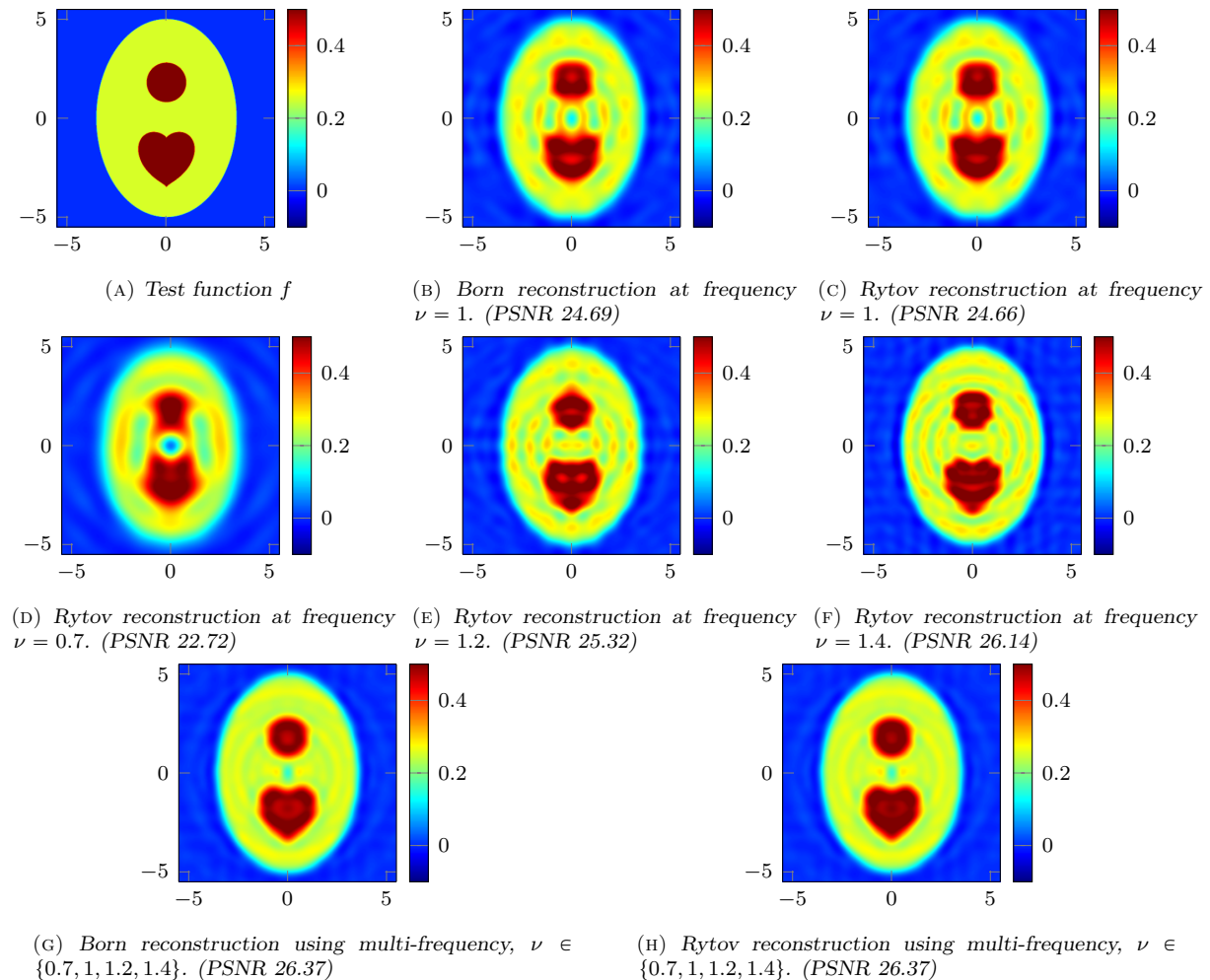


FIGURE 16. Reconstructions for different frequencies of the incident wave. The PSNR is computed on the visible part of the grid for the real part of the reconstruction, since we know that  $f$  must be real.

Moreover, we consider the similar object of higher contrast from Figure 15a. Here, the reconstructions with Born and Rytov approximation differ more from the FWI reconstruction because of the more severe scattering, see Figure 17. In general, we can expect the FWI reconstruction to be better since it is a numerical approximation of the wave equation, of which the Born or Rytov approximations are just linearizations.

**7.3. Reconstruction of embedded non-convex shapes.** We now consider the case with combinations of convex and non-convex shapes included in the background medium.

**7.3.1. Reconstruction using FWI.** In Figure 18 and Figure 19, we show the model perturbation which consist in small objects buried in the background. FWI is carried out with single and multiple frequencies, while we investigate a mild contrast in Figure 18 (where  $f$  is at most 0.5) and a stronger contrast in Figure 19 (where  $f$  is at most 2). We see that the model can be recovered using a single frequency, which has to be selected depending on the contrast. As an

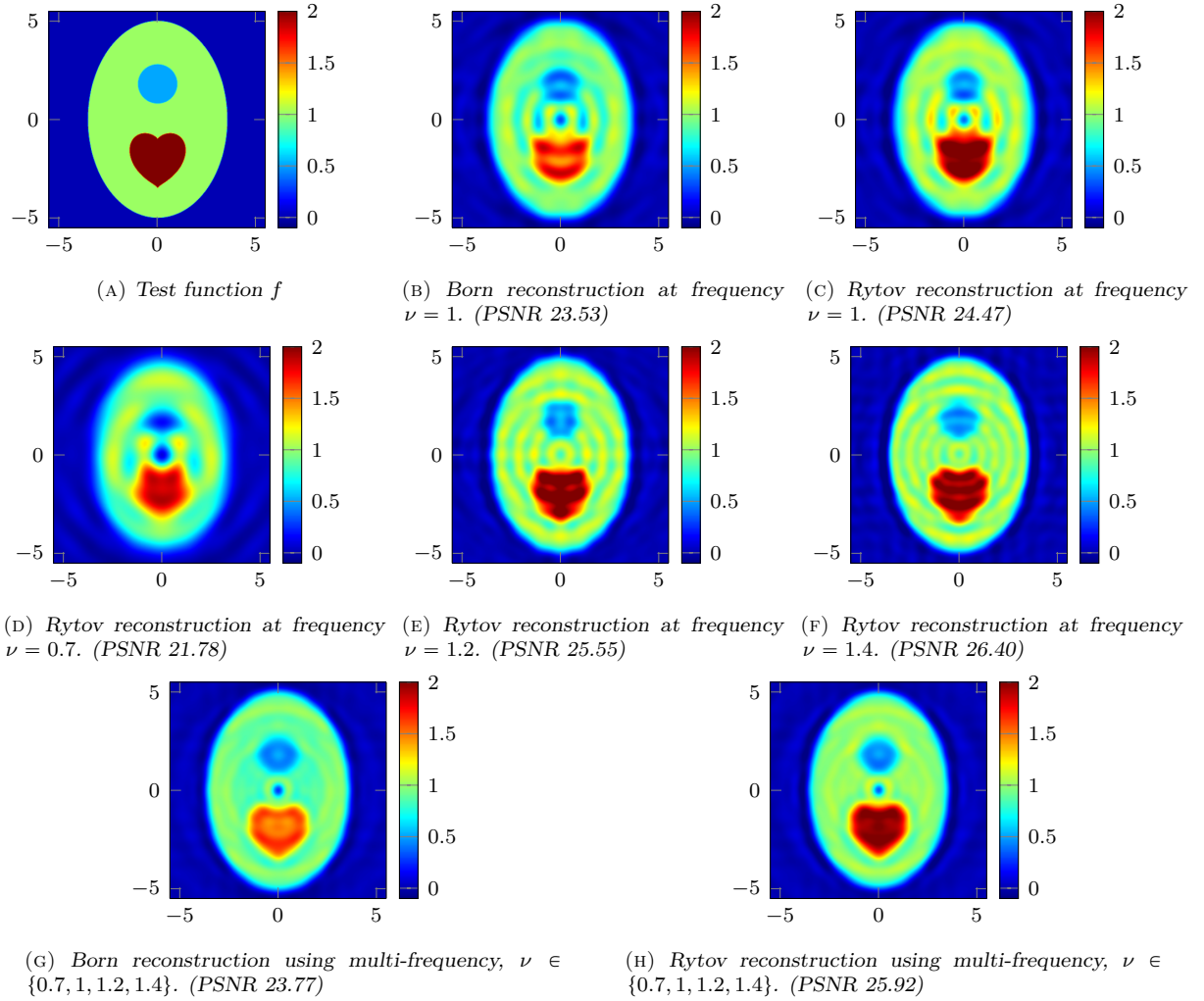


FIGURE 17. Reconstructions with a higher contrast, where the rest of the setting is the same as in Figure 16.

alternative, multi-frequency data appears to be a robust candidate and always provides a good reconstruction, for both the object's shape and amplitude.

**7.3.2. Reconstruction using Born and Rytov approximations.** In Figure 20, we show the reconstruction using Born and Rytov approximations. Here, we can clearly see that we need a higher frequency in order to resolve small features of the object.

With a higher contrast, the reconstruction with the Rytov approximation is considerably better than the one with the Born approximation, see Figure 21. This is consistent with Remark 3.1. Interestingly, the shapes reconstruction in high contrast barely profits from taking frequencies higher than 1, even though the Fourier space coverage is larger.

#### 7.4. Computational costs.

**Computational cost of FWI.** The computational cost of FWI comes from the discretization and resolution of the wave problem Equation 3.12 for each of the sources in the acquisition, coupled with the iterative procedure of Algorithm 1. In our numerical experiments, we use

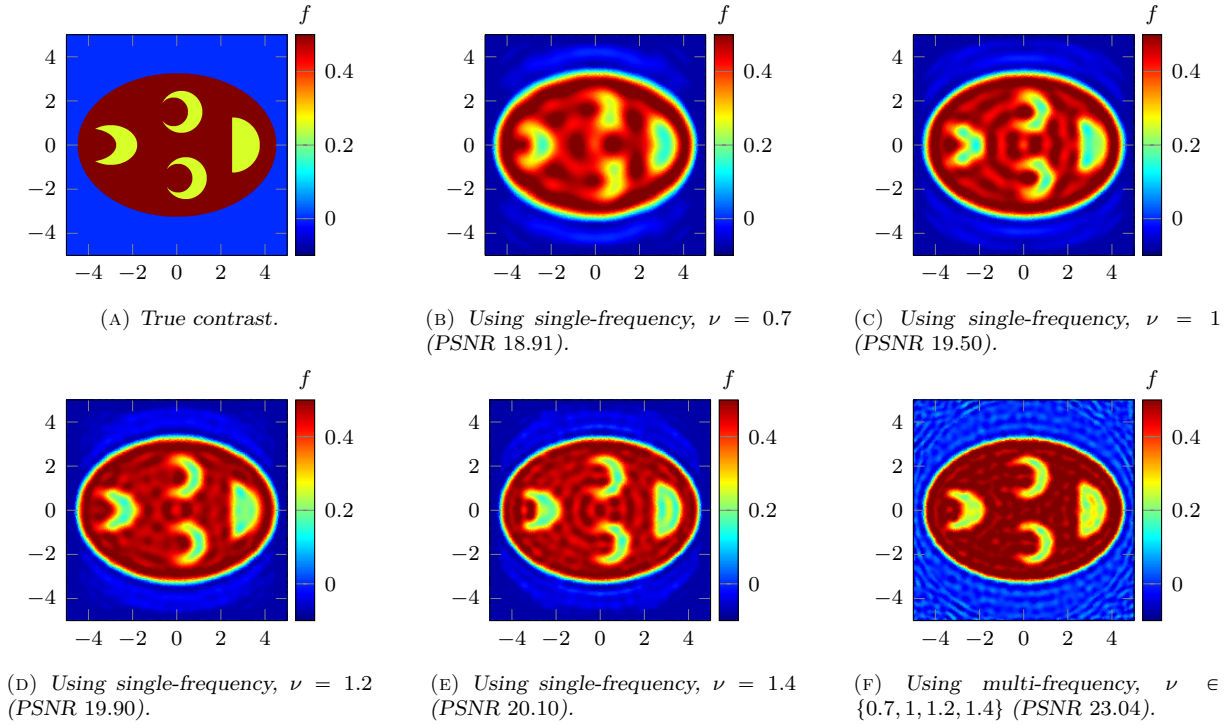


FIGURE 18. Reconstruction with FWI starting from a homogeneous background with  $f = 0$ . The models are given at frequency  $\nu = 1$  and the wave-speed is equal to 1 in the background.

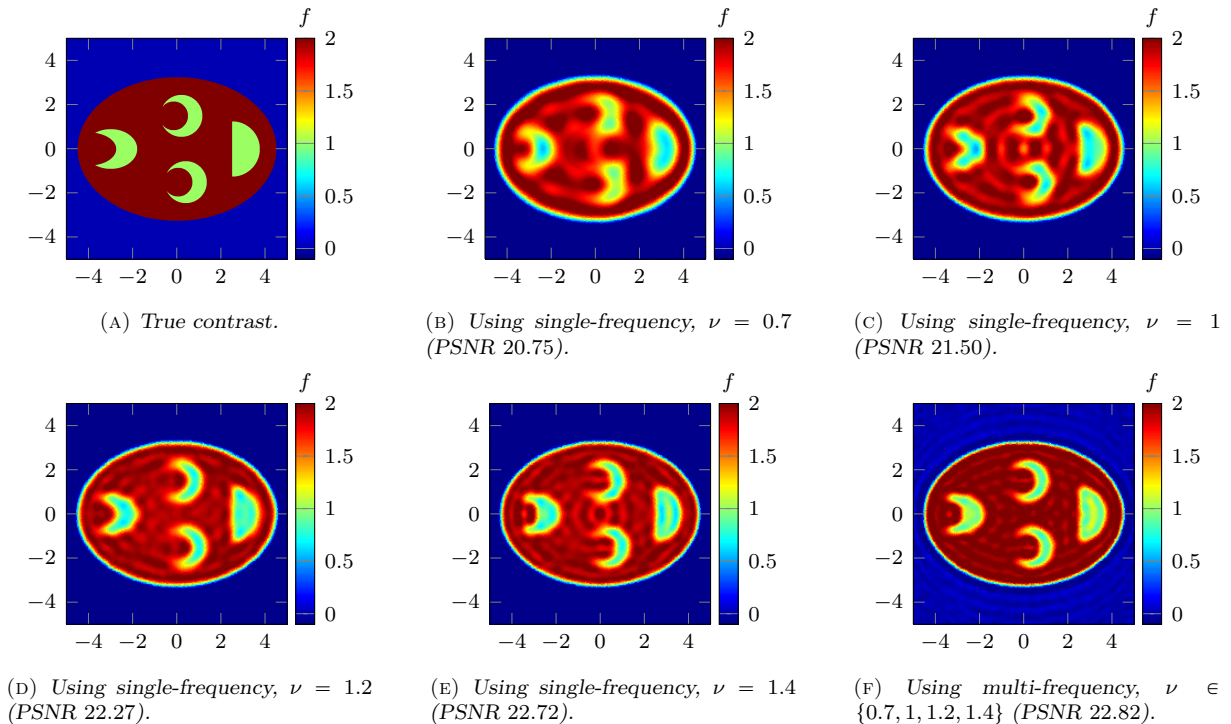


FIGURE 19. Reconstruction with FWI starting from a homogeneous background with  $f = 0$ . The models are given at frequency  $\nu = 1$  and the wave-speed is equal to 1 in the background.

the software `hawen` for the iterative inversion, [14], footnote 1, which relies on the Hybridizable discontinuous Galerkin discretization. The number of degrees of freedom for the discretization

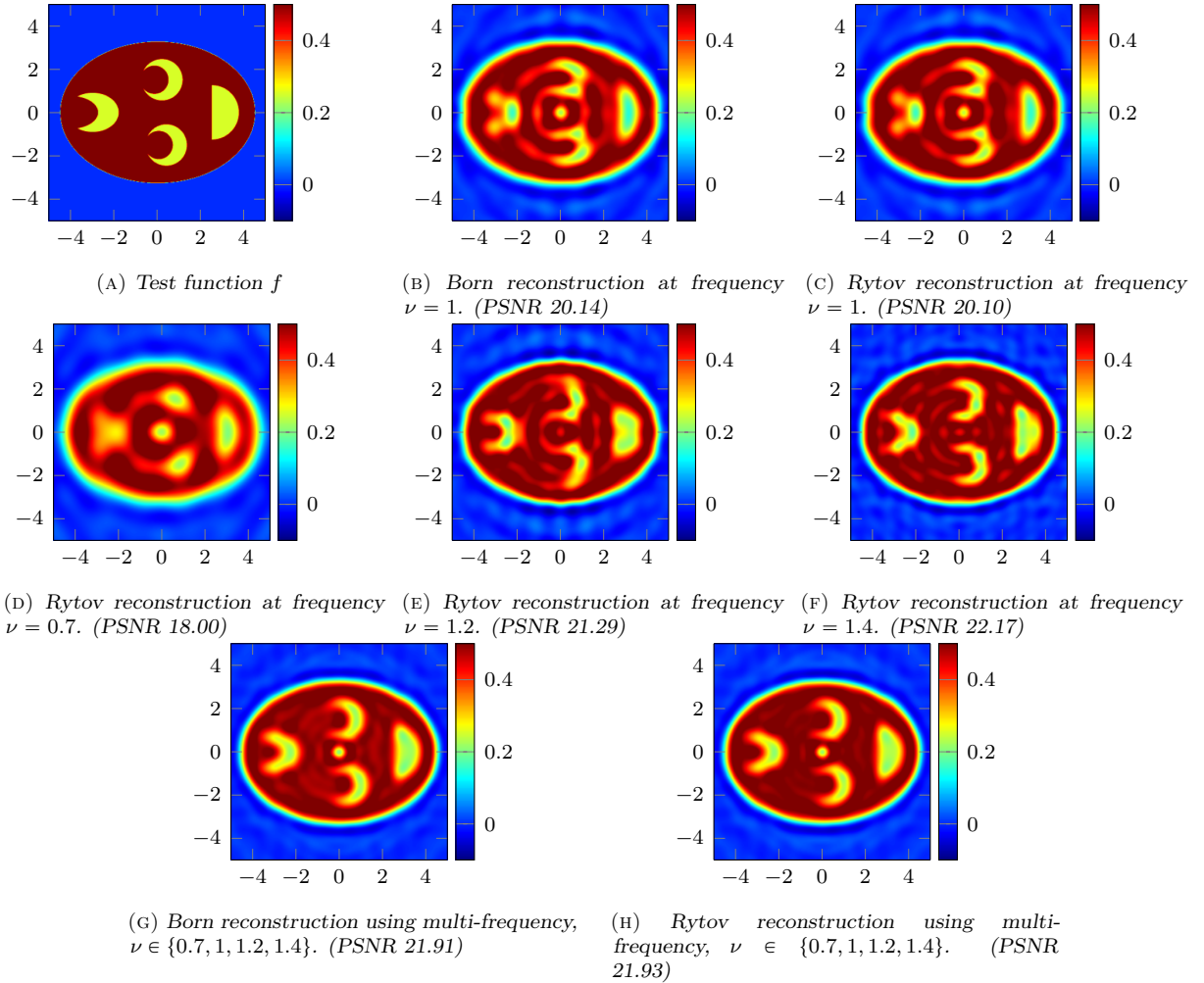


FIGURE 20. Reconstructions of the more complicated shapes. The models are given at frequency  $\nu = 1$ .

depends on the polynomial order, which is selected depending on the wavelength, see [18]. For the resolution of the wave equation for multiple sources, the linear system resulting from the discretization of Equation 3.12 is solved with the direct solver MUMPS, [1]. Once the matrix factorization is computed, the numerical cost of having several sources (i.e., multiple right-hand sides in the linear system) is drastically mitigated, hence motivating the use of a direct solver instead of an iterative one.

Our numerical experiments have been carried out on the Vienna Scientific Cluster VSC-4<sup>2</sup>, using 48 cores. For the reconstructions of Figure 14, Figure 15, Figure 18 and Figure 19, the size of the computational domain is  $40 \times 40$ , with about 350 000 degrees of freedom. Using single-frequency data, 50 iterations are performed in Algorithm 1 and the total computational time is of about 40 min. In the case of multiple frequencies, we have a total of 120 iterations and the computational time is of about 1 h 45 min.

**Computational cost of Born and Rytov approximations.** The conjugate gradient method used in the inverse NDFT requires in each iteration step the evaluation of an NDFT Equation 6.8 and its adjoint. We utilize the nonequispaced fast Fourier transform (NFFT) algorithm [29], implemented in the open-source software library `nfft` [28], which can compute an NDFT in

<sup>2</sup><https://vsc.ac.at/>

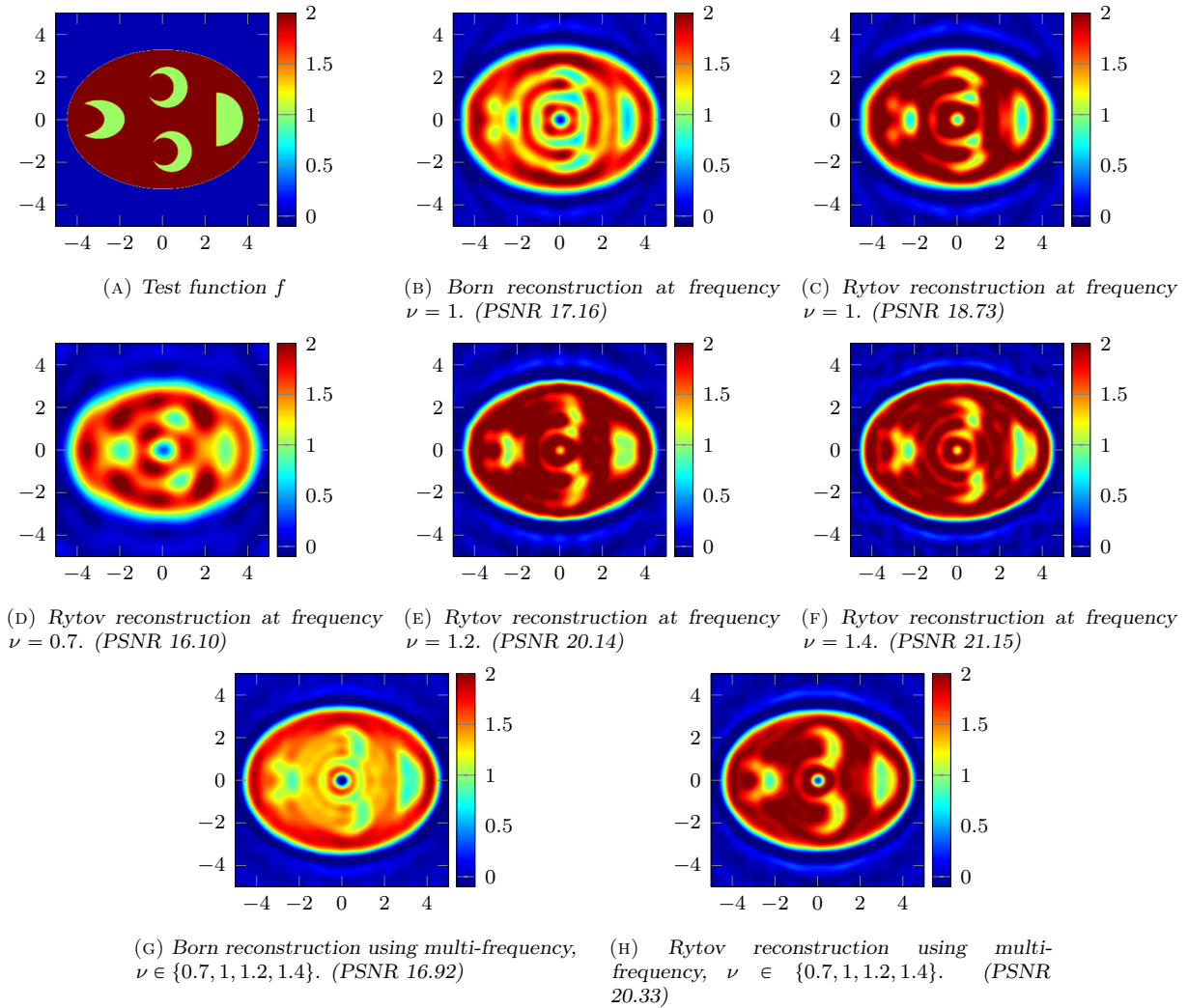


FIGURE 21. Reconstructions of the more complicated shapes with a higher contrast than in Figure 20. The models are given at frequency  $\nu = 1$ .

$\mathcal{O}(N^2 \log N + M)$  arithmetic operations, which is considerably less than the  $\mathcal{O}(N^2 M)$  operations of a straightforward implementation of Equation 6.8.

The numerical simulations of subsection 7.2.2 have been carried out on a 4-core Intel Core i5-6500 processor. We used 12 iterations of the conjugate gradient method and noted that the reconstruction quality hardly benefits from a higher number of iterations. The reconstruction of an image took about one second, with a grid size  $720 \times 720$  of  $f$  and  $200 \times 100$  data points of  $u$  for each frequency. Therefore, the numerical computation of the Born and Rytov approximations is much faster than the FWI.

## 8. CONCLUSION

We study the imaging problem for diffraction tomography, where wave measurements are used to quantitatively reconstruct the physical properties, i.e., the refractive index. The forward operator that describes the wave propagation corresponds with the Helmholtz equation, which, under the assumption of small background perturbations, can be represented via the Born and Rytov

approximations.

Firstly, we have compared different forward models in terms of the resulting measured data  $u$ . It highlights that, even in the case of a small circular object, the Born approximation is not entirely accurate to represent the total wave field given by the Helmholtz equation. In addition, the source that initiates the phenomenon (e.g., a point source located very far from the object, or simultaneous point source along a line), also plays an important role as it changes the resulting signals, hence leading to systematic differences depending on the choice of forward model. We found that the line source model approximates the plane wave pretty well.

Secondly, we have carried out the reconstruction using data from the total field  $u^{\text{tot}}$ , and compared the efficiency of the Full Waveform Inversion method (FWI) with that of the Born and Rytov approximations. FWI works directly with the Helmholtz problem, Equation 3.12, hence giving a robust approach that can be implemented in all configurations, however at the cost of possibly intensive computations. On the other hand, the Born and Rytov are computationally cheap, but lack accuracy when the object is too large or when the contrast is too strong. We have also noted that the Rytov approximation gives better results than the Born one. Furthermore, for all reconstruction methods, we have shown that using data of multiple frequencies allows to improve the robustness of the reconstruction by providing information on multiple wavelengths.

**Acknowledgments.** This work is supported by the Austrian Science Fund (FWF) within SFB F68 (“Tomography across the Scales”), Projects F68-06 and F68-07. FF is funded by the Austrian Science Fund (FWF) under the Lise Meitner fellowship M 2791-N. Funding by the DFG under Germany’s Excellence Strategy – The Berlin Mathematics Research Center MATH+ (EXC-2046/1, Projektnummer: 390685689) is gratefully acknowledged. For the numerical experiments, we acknowledge the use of the Vienna Scientific Cluster VSC-4 (<https://vsc.ac.at/>).

## REFERENCES

- [1] P. R. Amestoy, A. Buttari, J.-Y. L’excellent, and T. Mary. “Performance and scalability of the block low-rank multifrontal factorization on multicore architectures”. In: *ACM Transactions on Mathematical Software (TOMS)* 45.1 (2019), pp. 1–26. DOI: [10.1145/3242094](https://doi.org/10.1145/3242094) (cited on page 25).
- [2] A. Bamberger, G. Chavent, and P. Lailly. “About the stability of the inverse problem in the 1-d wave equation”. In: *Journal of Applied Mathematics and Optimisation* 5 (1979), pp. 1–47 (cited on pages 2, 11).
- [3] H. Barucq, G. Chavent, and F. Faucher. “A priori estimates of attraction basins for nonlinear least squares, with application to Helmholtz seismic inverse problem”. In: *Inverse Problems* 35.11 (11 2019), p. 115004. DOI: [10.1088/1361-6420](https://doi.org/10.1088/1361-6420) (cited on page 12).
- [4] J. B. Bednar, C. Shin, and S. Pyun. “Comparison of waveform inversion, part 2: phase approach”. In: *Geophysical Prospecting* 55 (4 2007), pp. 465–475. ISSN: 1365-2478. DOI: [10.1111/j.1365-2478.2007.00618.x](https://doi.org/10.1111/j.1365-2478.2007.00618.x) (cited on page 12).
- [5] C. Bunks, F. M. Saleck, S. Zaleski, and G. Chavent. “Multiscale seismic waveform inversion”. In: *Geophysics* 60 (5 1995), pp. 1457–1473. DOI: [10.1190/1.1443880](https://doi.org/10.1190/1.1443880) (cited on pages 12, 16).

- [6] B. Chen and J. J. Stamnes. “Validity of diffraction tomography based on the first Born and the first Rytov approximations”. In: *Applied Optics* 37.14 (1998), p. 2996. DOI: [10.1364/ao.37.002996](https://doi.org/10.1364/ao.37.002996) (cited on pages 2, 5).
- [7] F. Clément, G. Chavent, and S. Gómez. “Migration-based traveltime waveform inversion of 2-D simple structures: A synthetic example”. In: *Geophysics* 66 (3 2001), pp. 845–860. DOI: [10.1190/1.1444974](https://doi.org/10.1190/1.1444974) (cited on page 13).
- [8] B. Cockburn, J. Gopalakrishnan, and R. Lazarov. “Unified hybridization of discontinuous Galerkin, mixed, and continuous Galerkin methods for second order elliptic problems”. In: *SIAM Journal on Numerical Analysis* 47.2 (2009), pp. 1319–1365. DOI: [10.1137/070706616](https://doi.org/10.1137/070706616) (cited on pages 3, 6).
- [9] D. Colton and R. Kress. “Inverse Acoustic and Electromagnetic Scattering Theory”. 3rd ed. Applied Mathematical Sciences 93. Berlin: Springer, 2013. ISBN: 978-1-4614-4941-6. DOI: [10.1007/978-1-4614-4942-3](https://doi.org/10.1007/978-1-4614-4942-3) (cited on page 5).
- [10] A. Devaney. “A filtered backpropagation algorithm for diffraction tomography”. In: *Ultrasonic Imaging* 4.4 (1982), pp. 336–350. DOI: [10.1016/0161-7346\(82\)90017-7](https://doi.org/10.1016/0161-7346(82)90017-7) (cited on page 2).
- [11] B. Engquist and A. Majda. “Absorbing boundary conditions for numerical simulation of waves”. In: *Proceedings of the National Academy of Sciences* 74.5 (1977), pp. 1765–1766 (cited on page 6).
- [12] S. Fan, S. Smith-Dryden, G. Li, and B. E. A. Saleh. “An iterative reconstruction algorithm for optical diffraction tomography”. In: *IEEE Photonics Conference (IPC)*. 2017, pp. 671–672. DOI: [10.1109/ipcon.2017.8116276](https://doi.org/10.1109/ipcon.2017.8116276) (cited on page 2).
- [13] F. Faucher. “Contributions to seismic full waveform inversion for time harmonic wave equations: Stability estimates, convergence analysis, numerical experiments involving large scale optimization algorithms”. PhD thesis. Université de Pau et Pays de l’Ardour, 2017, pp. 1–400 (cited on page 12).
- [14] F. Faucher. “**hawen**: time-harmonic wave modeling and inversion using hybridizable discontinuous Galerkin discretization”. In: *Journal of Open Source Software* 6 (57 2021). DOI: [10.21105/joss.02699](https://doi.org/10.21105/joss.02699) (cited on pages 3, 6, 15, 24).
- [15] F. Faucher, G. Alessandrini, H. Barucq, M. de Hoop, R. Gaburro, and E. Sincich. “Full Reciprocity-Gap Waveform Inversion, enabling sparse-source acquisition”. In: *Geophysics* 85.6 (2020), R461–R476. DOI: [10.1190/geo2019-0527.1](https://doi.org/10.1190/geo2019-0527.1) (cited on page 12).
- [16] F. Faucher, G. Chavent, H. Barucq, and H. Calandra. “A priori estimates of attraction basins for velocity model reconstruction by time-harmonic Full Waveform Inversion and Data-Space Reflectivity formulation”. In: *Geophysics* 85 (3 2020), R223–R241. DOI: [10.1190/geo2019-0251.1](https://doi.org/10.1190/geo2019-0251.1) (cited on pages 12, 13, 16).
- [17] F. Faucher, M. V. de Hoop, and O. Scherzer. “Reciprocity-gap misfit functional for Distributed Acoustic Sensing, combining data from passive and active sources”. In: *Geophysics* 86 (2 2021), R211–R220. ISSN: 0016-8033. DOI: [10.1190/geo2020-0305.1](https://doi.org/10.1190/geo2020-0305.1) (cited on page 12).
- [18] F. Faucher and O. Scherzer. “Adjoint-state method for Hybridizable Discontinuous Galerkin discretization, application to the inverse acoustic wave problem”. In: *Computer Methods in Applied Mechanics and Engineering* 372 (2020), p. 113406. ISSN: 0045-7825. DOI: [10.1016/j.cma.2020.113406](https://doi.org/10.1016/j.cma.2020.113406) (cited on pages 3, 6, 12, 25).
- [19] F. Faucher, O. Scherzer, and H. Barucq. “Eigenvector Models for Solving the Seismic Inverse Problem for the Helmholtz Equation”. In: *Geophysical Journal International* (Jan. 2020). ISSN: 0956-540X. DOI: [10.1093/gji/ggaa009](https://doi.org/10.1093/gji/ggaa009) (cited on pages 12, 19).

- [20] A. Fichtner, B. L. Kennett, H. Igel, and H.-P. Bunge. “Theoretical background for continental-and global-scale full-waveform inversion in the time–frequency domain”. In: *Geophysical Journal International* 175.2 (2 2008), pp. 665–685. DOI: [10.1111/j.1365-246X.2008.03923.x](https://doi.org/10.1111/j.1365-246X.2008.03923.x) (cited on page 12).
- [21] M. Hanke. “Conjugate Gradient Type Methods for Ill-Posed Problems”. Vol. 327. Pitman Research Notes in Mathematics Series. Harlow: Longman Scientific & Technical, 1995 (cited on page 14).
- [22] R. Hielscher, D. Potts, and M. Quellmalz. “An SVD in Spherical Surface Wave Tomography”. In: *New Trends in Parameter Identification for Mathematical Models*. Ed. by B. Hofmann, A. Leitao, and J. P. Zubelli. Trends in Mathematics. Basel: Birkhäuser, 2018, pp. 121–144. ISBN: 978-3-319-70823-2. DOI: [10.1007/978-3-319-70824-9\\_7](https://doi.org/10.1007/978-3-319-70824-9_7) (cited on page 2).
- [23] R. Hielscher and M. Quellmalz. “Optimal Mollifiers for Spherical Deconvolution”. In: *Inverse Problems* 31.8 (2015), p. 085001. DOI: [10.1088/0266-5611/31/8/085001](https://doi.org/10.1088/0266-5611/31/8/085001) (cited on page 2).
- [24] R. Hielscher and M. Quellmalz. “Reconstructing a Function on the Sphere from Its Means Along Vertical Slices”. In: *Inverse Probl. Imaging* 10.3 (2016), pp. 711–739. ISSN: 1930-8337. DOI: [10.3934/ipi.2016018](https://doi.org/10.3934/ipi.2016018) (cited on page 2).
- [25] K. Iwata and R. Nagata. “Calculation of Refractive Index Distribution from Interferograms Using the Born and Rytov’s Approximation”. In: *Japanese Journal of Applied Physics* 14.S1 (Jan. 1975), pp. 379–383. DOI: [10.7567/jjaps.14s1.379](https://doi.org/10.7567/jjaps.14s1.379) (cited on page 2).
- [26] A. C. Kak and M. Slaney. “Principles of Computerized Tomographic Imaging”. Vol. 33. Classics in Applied Mathematics. Philadelphia, PA: Society for Industrial and Applied Mathematics (SIAM), 2001 (cited on pages 5, 9).
- [27] B. Kaltenbacher. “Minimization Based Formulations of Inverse Problems and Their Regularization”. In: *SIAM Journal on Optimization* 28.1 (2018), pp. 620–645. DOI: [10.1137/17M1124036](https://doi.org/10.1137/17M1124036) (cited on page 12).
- [28] J. Keiner, S. Kunis, and D. Potts. *NFFT 3.5, C subroutine library*. <https://www.tu-chemnitz.de/~potts/nfft> (cited on page 25).
- [29] J. Keiner, S. Kunis, and D. Potts. “Using NFFT3 - a Software Library for Various Nonequispaced Fast Fourier Transforms”. In: *ACM Trans. Math. Software* 36 (2009), Article 19, 1–30. DOI: [10.1145/1555386.1555388](https://doi.org/10.1145/1555386.1555388) (cited on page 25).
- [30] C. Kirisits, M. Quellmalz, M. Ritsch-Martel, O. Scherzer, E. Setterqvist, and G. Steidl. “Fourier reconstruction for diffraction tomography of an object rotated into arbitrary orientations”. In: *Inverse Problems* (2021). ISSN: 0266-5611. DOI: [10.1088/1361-6420/ac2749](https://doi.org/10.1088/1361-6420/ac2749) (cited on pages 2, 13).
- [31] T. Knopp, S. Kunis, and D. Potts. “A note on the iterative MRI reconstruction from nonuniform k-space data”. In: *Int. J. Biomed. Imag.* 2007 (2007). DOI: [10.1155/2007/24727](https://doi.org/10.1155/2007/24727) (cited on page 2).
- [32] S. Kunis and D. Potts. “Stability results for scattered data interpolation by trigonometric polynomials”. In: *SIAM J. Sci. Comput.* 29 (2007), pp. 1403–1419. DOI: [10.1137/060665075](https://doi.org/10.1137/060665075) (cited on page 14).
- [33] P. Lailly. “The seismic inverse problem as a sequence of before stack migrations”. In: *Conference on Inverse Scattering: Theory and Application*. Ed. by J. B. Bednar. Society for Industrial and Applied Mathematics, 1983, pp. 206–220 (cited on pages 2, 11).
- [34] Y. Luo and G. T. Schuster. “Wave-equation traveltime inversion”. In: *Geophysics* 56.5 (1991), pp. 645–653. DOI: [10.1190/1.1443081](https://doi.org/10.1190/1.1443081) (cited on page 12).

- [35] L. Métivier, R. Brossier, Q. Mérigot, E. Oudet, and J. Virieux. “Measuring the misfit between seismograms using an optimal transport distance: application to full waveform inversion”. In: *Geophysical Journal International* 205.1 (2016), pp. 345–377. DOI: [10.1093/gji/ggw014](https://doi.org/10.1093/gji/ggw014) (cited on page 12).
- [36] P. Müller, M. Schürmann, and J. Guck. *The Theory of Diffraction Tomography*. 2016. arXiv: [1507.00466 \[q-bio.QM\]](https://arxiv.org/abs/1507.00466) (cited on page 18).
- [37] P. Müller, M. Schürmann, and J. Guck. “ODTbrain: a Python library for full-view, dense diffraction tomography”. In: *BMC Bioinformatics* 16 (367 2015). DOI: [DOI10.1186/s12859-015-0764-0](https://doi.org/10.1186/s12859-015-0764-0) (cited on pages 2, 14).
- [38] F. Natterer and F. Wübbeling. “Mathematical Methods in Image Reconstruction”. Monographs on Mathematical Modeling and Computation 5. Philadelphia, PA: SIAM, 2001 (cited on page 9).
- [39] J. Nocedal and S. J. Wright. “Numerical Optimization”. 2nd ed. Springer Series in Operations Research, 2006 (cited on page 12).
- [40] R.-E. Plessix. “A review of the adjoint-state method for computing the gradient of a functional with geophysical applications”. In: *Geophysical Journal International* 167.2 (2 2006), pp. 495–503. DOI: [10.1111/j.1365-246X.2006.02978.x](https://doi.org/10.1111/j.1365-246X.2006.02978.x) (cited on page 12).
- [41] G. Plonka, D. Potts, G. Steidl, and M. Tasche. “Numerical Fourier Analysis”. Applied and Numerical Harmonic Analysis. Birkhäuser, 2018. ISBN: 978-3-030-04305-6. DOI: [10.1007/978-3-030-04306-3](https://doi.org/10.1007/978-3-030-04306-3) (cited on page 14).
- [42] D. Potts and G. Steidl. “A new linogram algorithm for computerized tomography”. In: *IMA J. Numer. Anal.* 21 (2001), pp. 769–782. DOI: [10.1093/imanum/21.3.769](https://doi.org/10.1093/imanum/21.3.769) (cited on page 2).
- [43] R. G. Pratt, C. Shin, and G. J. Hick. “Gauss–Newton and full Newton methods in frequency–space seismic waveform inversion”. In: *Geophysical Journal International* 133.2 (1998), pp. 341–362. DOI: [10.1046/j.1365-246X.1998.00498.x](https://doi.org/10.1046/j.1365-246X.1998.00498.x) (cited on pages 2, 11, 12).
- [44] S. Pyun, C. Shin, and J. B. Bednar. “Comparison of waveform inversion, part 3: amplitude approach”. In: *Geophysical Prospecting* 55 (4 2007), pp. 477–485. ISSN: 1365-2478. DOI: [10.1111/j.1365-2478.2007.00619.x](https://doi.org/10.1111/j.1365-2478.2007.00619.x) (cited on page 12).
- [45] C. Shin, S. Pyun, and J. B. Bednar. “Comparison of waveform inversion, part 1: conventional wavefield vs logarithmic wavefield”. In: *Geophysical Prospecting* 55 (4 2007), pp. 449–464. ISSN: 1365-2478. DOI: [10.1111/j.1365-2478.2007.00617.x](https://doi.org/10.1111/j.1365-2478.2007.00617.x) (cited on page 12).
- [46] M. Slaney, A. Kak, and L. Larsen. “Limitations of Imaging with First-Order Diffraction Tomography”. In: *IEEE Transactions on Microwave Theory and Techniques* 32.8 (1984), pp. 860–874. DOI: [10.1109/TMTT.1984.1132783](https://doi.org/10.1109/TMTT.1984.1132783) (cited on pages 2, 5).
- [47] Y. Sung, W. Choi, C. Fang-Yen, K. Badizadegan, R. R. Dasari, and M. S. Feld. “Optical diffraction tomography for high resolution live cell imaging”. In: *Optics express* 17.1 (2009), pp. 266–277 (cited on page 2).
- [48] A. Tarantola. “Inversion of seismic reflection data in the acoustic approximation”. In: *Geophysics* 49 (1984), pp. 1259–1266. DOI: [10.1190/1.1441754](https://doi.org/10.1190/1.1441754) (cited on pages 2, 11).
- [49] T. Van Leeuwen and W. Mulder. “A correlation-based misfit criterion for wave-equation travelttime tomography”. In: *Geophysical Journal International* 182.3 (2010), pp. 1383–1394 (cited on page 12).
- [50] J. Virieux and S. Operto. “An overview of full-waveform inversion in exploration geophysics”. In: *Geophysics* 74 (6 2009), WCC1–WCC26. DOI: [10.1190/1.3238367](https://doi.org/10.1190/1.3238367) (cited on pages 2, 11, 12).

- 
- [51] E. Wolf. “Three-dimensional structure determination of semi-transparent objects from holographic data”. In: *Optics Communications* 1 (1969), pp. 153–156 (cited on pages [2](#), [9](#)).